Clim Dyn
DOI 10.1007/s00382-010-0867-2

Sahel rainfall and decadal to multi-decadal sea surface temperature variability

Elsa Mohino · Serge Janicot · Juergen Bader

Received: 21 December 2009 / Accepted: 11 June 2010
© Springer-Verlag 2010

Abstract Decadal Sahelian rainfall variability was mainly driven by sea surface temperatures (SSTs) during the twentieth century. At the same time SSTs showed a marked long-term global warming (GW) trend. Superimposed on this long-term trend decadal and multi-decadal variability patterns are observed like the Atlantic Multidecadal Oscillation (AMO) and the inter-decadal Pacific Oscillation (IPO). Using an atmospheric general circulation model we investigate the relative contribution of each component to the Sahelian precipitation variability. To take into account the uncertainty related to the use of different SST data sets, we perform the experiments using HadISST1 and ERSSTv3 reconstructed sets. The simulations show that all three SST signals have a significant impact over West Africa: the positive phases of the GW and the IPO lead to drought over the Sahel, while a positive AMO enhances Sahel rainfall. The tropical SST warming is the main cause for the GW impact on Sahel rainfall. Regarding the AMO, the pattern of anomalous precipitation is established by the SSTs in the Atlantic and Mediterranean basins. In turn, the tropical SST anomalies control the impact of the IPO component on West Africa. Our results suggest that the low-frequency evolution of Sahel rainfall can be interpreted as the competition of three factors: the effect of the GW, the AMO and the IPO. Following this interpretation, our results show that 50% of the SST-driven Sahel drought in the 1980s is explained by the change to a negative phase of the AMO, and that the GW contribution was 10%. In addition, the partial recovery of Sahel rainfall in recent years was mainly driven by the AMO.

Keywords Decadal variability · Sea surface temperatures · West African Monsoon · Atmospheric general circulation models

E. Mohino (✉)
LOCEAN/IPSL, CNRS, Université Pierre et Marie Curie, Paris, France
e-mail: emohino@fis.ucm.es

E. Mohino
Universidad de Sevilla, Seville, Spain

S. Janicot
LOCEAN/IPSL, IRD, Université Pierre et Marie Curie, Paris, France

J. Bader
Bjerknes Centre for Climate Research, Bergen, Norway

J. Bader
Geophysical Institute, University of Bergen, Bergen, Norway

1 Introduction

Precipitation over the Sahel shows pronounced decadal variability and a negative trend between wet conditions in the 1950s and 1960s to dry ones in the 1970s and 1980s (Fig. 1a). A number of studies highlight the instrumental role of sea surface temperatures (SST) in driving such variability (e.g. Folland et al. 1986; Palmer 1986; Rowell et al. 1992; Giannini et al. 2003; Lu and Delworth 2005). Land–atmosphere interactions act as an amplification of such a signal (Zeng et al. 1999; Giannini et al. 2003; Yoshioka et al. 2007).

During the second half of the twentieth century there was a decrease in precipitation in the whole monsoon system (Zhou et al. 2008). However, the negative trend in the Sahel is outstanding. This led to qualify its drought as one of the largest climate changes anywhere else (Trenberth et al. 2007). The warming shown over the tropical

Published online: 27 June 2010

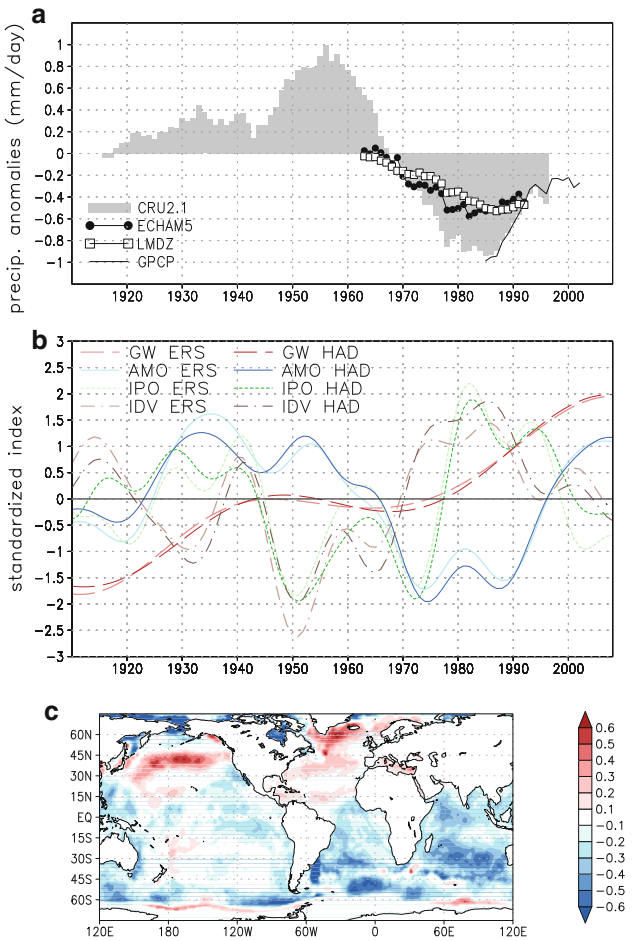

Fig. 1 **a** Low-frequency filtered (using a 13-year running mean) anomalies of precipitation (in mm/day) averaged over the Sahel (averaged between July and September and over the area 15W–15E and 10N–17N) are shown for the 1910–2002 CRUTS2.1 and 1979–2007 GPCP data sets in *bars* and *thin black line*, respectively, and for the 1957–1998 simulations with LMDZ (*squares*) and ECHAM5 (*circles*) models. All precipitation anomalies have been levelled to the CRUTS2.1 1910–2002 climatology. **b** The 1910–2008 standardized GW, AMO, IPO and IDV indices obtained with ERSSTv3 (HadISST1) data sets are shown in *light (strong) red long dashed*, *light (strong) blue solid lines*, *light (strong) green short dashed* and *light (strong) brown dot dash lines*, respectively. For the definition of each index see details in the text. **c** Inter-hemispheric pattern calculated as the regression of HadISST1 SSTs onto the low-frequency filtered (using a 13-year running mean) anomalies of CRUTS2.1 precipitation (units are K per standard deviation)

oceans and associated with the world-wide warming trend of SSTs is related to the Sahel drying (Lu and Delworth 2005). Among them, the tropical Indian (Bader and Latif 2003; Giannini et al. 2003; Lu and Delworth 2005) and tropical Pacific (Lu and Delworth 2005; Caminade and Terray 2009) are suggested to have the dominant role.

Biasutti and Giannini (2006) show that most of CMIP3 (third phase of the Coupled Intercomparison Project) coupled models dry the Sahel in the twentieth century when driven with observed external boundary conditions (natural and anthropogenic) with respect to preindustrial IPCC runs. Their results suggest that at least 30% of this drying is caused by external forcing due to the SST warming. In contrast, Hoerling et al. (2006) cannot explain neither the pattern nor the amplitude of the Sahelian drought by anthropogenic forcing.

During the twentieth century, Sahel precipitation showed decadal changes that cannot be solely explained by the global warming (GW) SST trend. Decadal/multi-decadal Sahel precipitation variability is positively linked to an inter-hemispheric SST contrast pattern (Folland et al. 1986) with warmer temperatures in the northern and cooler in the southern hemisphere (Fig. 1c). This suggests that other sources of decadal variability could be important for the the low-frequency evolution of Sahel rainfall.

In the Atlantic basin, the inter-hemispheric SST pattern is reminiscent of the Atlantic Multidecadal Oscillation (AMO). The AMO is a large-scale pattern of variability connected to the oceanic meridional overturning circulation (Knight et al. 2005). It shows a periodicity of about 50–70 year (Kerr 2000). The positive phase of the AMO is associated with warmer (cooler) than average SST over the North (South) Atlantic Ocean. The positive phase of the AMO is associated with increased hurricane activity over the Atlantic (Zhang and Delworth 2006; Trenberth and Shea 2006; Knight et al. 2006), decreased precipitation over northern South America (Knight et al. 2006) and decreased (increased) summer sea level pressure (surface temperature) over North America (Sutton and Hodson 2005). Studies relate increased Sahelian rainfall to the positive AMO phase (Folland et al. 1986; Rowell et al. 1995; Zhang and Delworth 2006; Knight et al. 2006; Ting et al. 2009), due to a northward displacement of the Inter-Tropical Convergence Zone (Knight et al. 2006). Shanahan et al. (2009) find that intervals of severe drought lasting for periods ranging from decades to centuries are related to the AMO over the past three millennia.

Over the Pacific, the inter-hemispheric pattern shows resemblance to the negative phase of the inter-decadal Pacific Oscillation (IPO) (Zhang et al. 1997). The IPO is the basin-wide pattern of the main mode of SST variability in the Pacific at decadal time scale. When focusing only on the North Pacific, this mode is called the Pacific Decadal Oscillation (Mantua et al. 1997). The main fingerprint of the positive phase of the IPO pattern is a cooling in the extra-tropics, mainly in the Northern Pacific sector, and a warming in the tropics. The actual mechanism producing the IPO is still under discussion (Mantua and Hare 2002). Several studies relate it to an internal mode (Meehl et al. 2009), in which coupled air–sea processes involve the tropical and mid latitude sectors (Meehl and Hu 2006; Desser et al. 2004). The IPO affects Australian rainfall (Power et al.

1999). Long-lived drought conditions over the Indian subcontinent and over North America are associated with an IPO-like pattern of SSTs (Krishnan and Sugi 2003; Meehl and Hu 2006). Joly (2008) shows a statistical link between Sahelian rainfall and the positive phase of the IPO.

The inter-hemispheric pattern shows high loadings over the Indian Ocean basin. This basin shows decadal timescale variability (Ashok et al. 2004), though some works (Cole et al. 2000; Crueger et al. 2009) suggest that this variability is highly related to the IPO. In this work we refer to it as Indian decadal variability (IDV).

Though the SST-driven variability of Sahel rainfall is the subject of numerous studies (Giannini et al. 2003; Bader and Latif 2003; Lu and Delworth 2005; Hoerling et al. 2006; Hagos and Cook 2008; Caminade and Terray 2009), the relative contribution of the different components of SST evolution is not yet quantified. This approach is a key to understand passed evolution of Sahelian rainfall and to assess more confidence in future scenarios. Therefore, we investigate the relative contribution to West African precipitation of the long-term GW trend of SSTs, the decadal and multi-decadal variability in the Atlantic (AMO) and the Pacific (IPO) basins. We perform SST-sensitivity experiments with the atmospheric general circulation model LMDZ. For the analysis and the simulations we use two different SST data sets: ERSSTv3 (Smith et al. 2008) and HadISST1 (Rayner et al. 2003). The paper is divided as follows. Section 2 presents the data used and the methodology followed. The components of the low-frequency variability of SSTs are analysed in Sect. 3. Their relationship with observed rainfall is also studied in Sect. 3.2. The performance of the model for simulating low-frequency variability of Sahel rainfall variability is addressed in Sect. 4. In this same section the analysis of the different simulations is given. Section 5 is devoted to the understanding the 1980s drought over the Sahel and its partial recovery in recent years. The caveats and limitations of this work are discussed in Sect. 6. Finally, the summary and conclusions are given in Sect. 7.

2 Data and methods

2.1 Observations

Two observational rainfall data-sets are used. One is the gauge based CRU TS 2.1 data-set (Mitchel and Jones 2005). It is a land-only global, gridded, monthly data-set. The spatial resolution is $0.5° \times 0.5°$. It covers the period 1901–2002. For the recent period, version 2 of the Global Precipitation Climatology Project (GPCP) data set (Adler et al. 2003) is used. It is a global, gridded, monthly data set with a spatial resolution of $2.5° \times 2.5°$ and available from 1979 onwards.

Our main focus is on the Sudano-Sahel area, defined as the latitudinal strap spanning the African continent from 10N to 20N. In the following we will refer to it as Sahel.

SST data sets differ in the strength of trends in certain oceanic regions (Vecchi et al. 2008; Falvey and Garreaud 2009). This could have an impact on the modelled rainfall. To address this source of uncertainty, two SST data sets are chosen, the HadISST1 (Rayner et al. 2003) and the ERSSTv3 (Smith et al. 2008). They are reconstructed monthly SST and sea ice fields. They have a global coverage and are gridded with a horizontal resolution of $1° \times 1°$ and $2° \times 2°$ for the HadISST1 and the ERSSTv3, respectively. They span the period from 1870 to present for HadISST1 and from 1854 onwards for the ERSSTv3 data set. The data sets differ in the in situ input data. HadISST1 is primarily based on observations from the Met Office Marine Data bank and uses monthly median SSTs from Comprehensive Ocean–Atmosphere Data Set (COADS) up to 1995 to enhance data coverage. ERSSTv3 is based on the International Comprehensive Ocean–Atmosphere Data Set (ICOADS) SST anomalies (Worley et al. 2005). Both data sets use night-time satellite-based data from the Advanced Very High Resolution Radiometer (AVHRR). They differ in the starting year (1985 for ERSSTv3 and 1982 for HadISST1) and only ERSSTv3 uses day-time satellite data. The algorithms for bias corrections of input data (in situ and satellite-based) are different. For instance, ERSSTv3 uses Smith and Reynolds (2002) methodology to correct the pre-1942 ship–buoy bias and HadISST1 uses Folland and Parker (1995) adjustment. For ERSSTv3 the reconstruction of the low-frequency is based on averaging data over large areas ($\sim 25°$) and filtering it over several years (between 5 and 15). Conversely, for HadISST1 the first empirical orthogonal function (EOF) of seasonal anomalies averaged over smaller areas ($\sim 4°$) is used and variations with periods smaller than 8 years are filtered out.

The analysis spans the period from 1910 to 2008. This period allows the study of decadal and multi-decadal signals while also ensuring enough SST data coverage.

2.2 Methodology

2.2.1 Indices

The GW index is based on yearly averaged global SSTs, which is a good approximation for the observed forced signal (Ting et al. 2009). Similarly to Baines and Folland (2007), we exclude the area above 60N and below 45S because of low SST data coverage. To remove decadal/multi-decadal variability and higher frequencies, the yearly time series is filtered using a Butterworth filter (order 10) with a cut-off period of 40 year. Following Trenberth et al. (2007), the 'minimum slope' constrain (Mann 2004) is

used to account for trends at the boundaries. This constrain reflects horizontally the time series at the ends and can be overly conservative regarding trends (Mann 2008). The 'adaptive' smoothing from Mann (2008) was tested and gave similar results.

The AMO, the IPO and the IDV indices are based on the leading principal components (PCs) of an EOF analysis. The computation is applied to yearly SSTs over the Atlantic, Pacific and Indian Ocean basins, respectively, between 45S and 60N. This approach is similar to Fontaine et al. (1998) except that they use global SSTs and not individual ocean basins. Like in Trenberth and Shea (2006) the GW signal is removed from the yearly SSTs before computing the EOFs. Since the GW is not spatially uniform, we follow a similar methodology as in Ting et al. (2009). We first define the yearly GW pattern as the projection of the yearly SSTs onto the GW index.

$$\mathrm{GWpat}_i = \sum \mathrm{SST}_i^j \cdot \mathrm{GWin}^j$$

where i is the spatial index, j the time index, SST_i^j the original SST data, GWin^j the GW index, previously defined and GWpat_i the yearly GW pattern.

For each year, the yearly GW pattern times the GW index is subtracted from the original SSTs to define the SST residual (SSTres_i^j):

$$\mathrm{SSTres}_i^j = \mathrm{SST}_i^j - \mathrm{GWpat}_i \cdot \mathrm{GWin}^j$$

To extract the decadal and multi-decadal scale variability, the residual SST data are filtered with a Butterworth low-pass filter of order 10 with a 13-year cut-off frequency before the EOF analysis. The 'minimum slope' constrain is used at the ends.

The anomalies are not standardized and the EOF analysis is applied to the co-variance matrix. The principal component associated with the first area weighted EOF over the Atlantic, Pacific and Indian basins respectively define the AMO, IPO and IDV indices. These first EOFs explain 42, 32 and 42% (37, 40 and 45%) of the total variance for the Atlantic, Pacific and Indian Ocean basins, respectively, using ERSSTv3 (HadISST1) residual data set. The first EOFs are significantly separated from the second ones according to the North et al. (1982) criterion.

2.2.2 Patterns

The GW, AMO, IPO and IDV associated global SST patterns are defined based on the regression of the observed global SSTs onto the 1910–2008 corresponding indices. To allow seasonal variations in the signals, observed monthly SST anomalies are regressed onto the yearly varying indices. This yields 12 monthly maps of SST anomalies for each component. Note that the regression patterns of the residual SSTs—after subtraction of the GW pattern—onto the AMO, IPO and IDV indices show no substantial differences, because of the weak correlation between the GW index and the AMO, IPO and IDV indices (Table 1). The GW, AMO, IPO and IDV indices show peaks at approximately ±2 standard deviations (Fig. 1b). To be representative of the peak behaviour, the associated SST patterns used in the SST-sensitivity experiments are defined as twice the regression maps. The summer (July–September) associated patterns are shown in Fig. 2. They correspond to the positive phase of the GW, AMO, IPO and IDV signals. The description of the regression patterns throughout the text agrees with the positive phase of the signals.

Table 1 Correlations between the GW, AMO, IPO and IDV indices

	GW	AMO	IPO	IDV
GW	0.997**	0.099	0.177	0.055
AMO	0.043	0.971**	-0.161	-0.578*
IPO	0.107	-0.198	0.878**	0.457*
IDV	0.129	-0.770**	0.515*	0.938**

Upper triangle (light shading) shows the correlation for the indices derived from the ERSSTv3 data set; lower triangle (dark shading) shows the correlation for the indices derived from the HadISST1 data set; the diagonal shows the correlation between the ERSSTv3 and HadISST1 derived indices. One (two) asterisk indicates 95% (99%) significant correlations

2.2.3 Model and experimental set-up

For the SST-sensitivity experiments we use version 4 of the LMDZ model. It is the atmospheric component of the IPSL-CM4 coupled model developed in the Institute Pierre Simon Laplace (Hourdin et al. 2006). One of the improvements with respect to the previous version 3 comes from the change of cloud and convection parametrizations. The use of a new parameterization scheme of moist convection (Emanuel 1991, 1993) improves the Hadley–Walker circulation. The cloud parameterization is coupled to the convective scheme using the approach followed by Bony and Emanuel (2001). This increases the back-scattering of solar radiation by convective clouds and improves convection over the continents. The model is run in standard configuration with a horizontal resolution of 3.75° in longitude and 2.5° in latitude, and 19 layers in the vertical.

In addition to the SST-sensitivity experiments a long-run simulation that spanned the 1957–1998 period is available for the LMDZ model. It is run in ensemble mode with six members using the monthly record of observed SSTs (Fiorino 2000) as boundary conditions. For comparison purposes we also use the output from a long-run done with the ECHAM5 model. This simulation consists of a five member ensemble run using observed SSTs (Latif

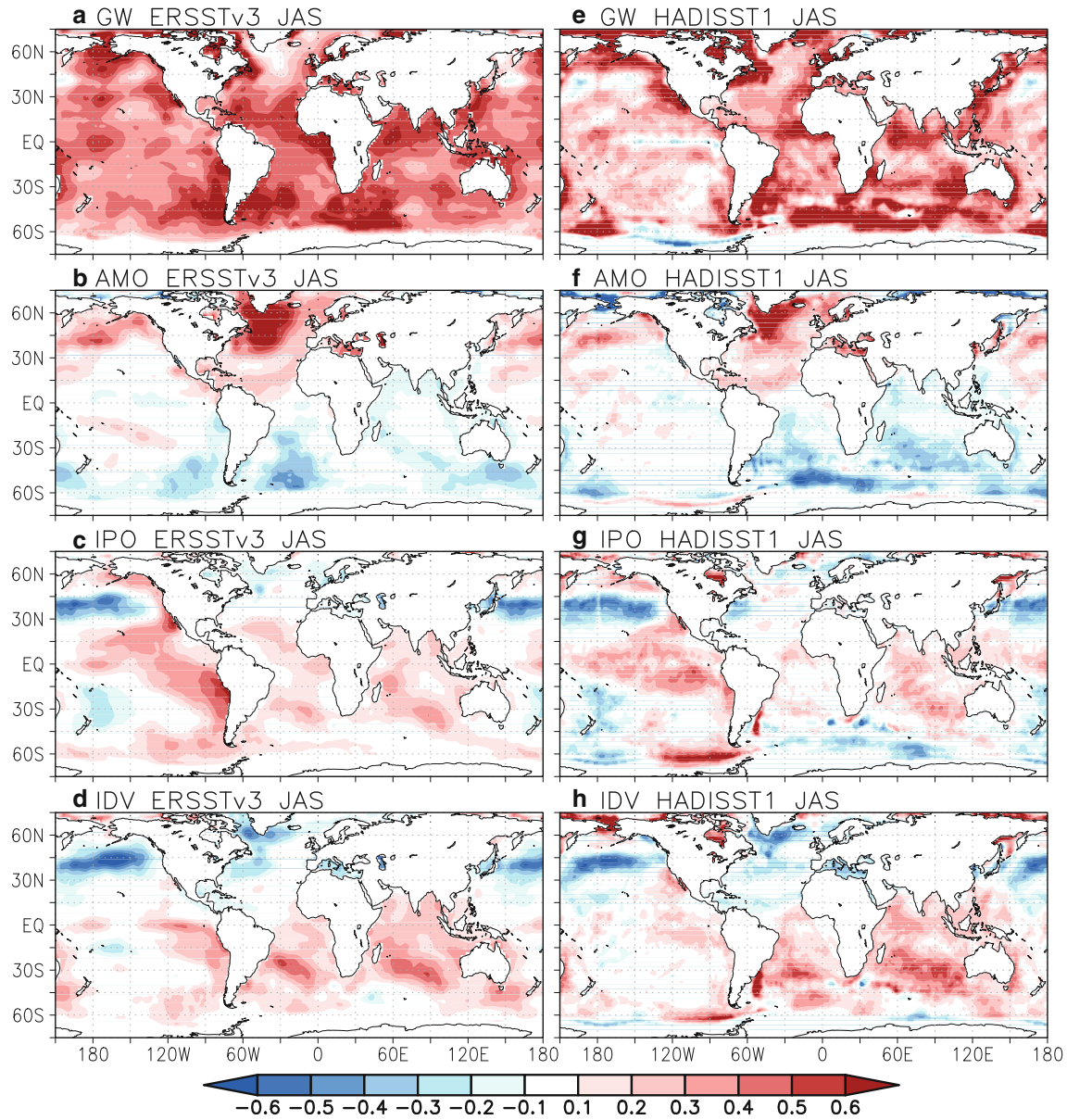

Fig. 2 July to September average of the associated patterns calculated from ERSSTv3 data set for: **a** the GW, **b** the AMO, **c** the IPO and **d** the IDV. Analogous patterns calculated from HadISST1 are shown in **e**–**h**. The monthly GW, AMO, IPO and IDV associated SST patterns were defined as twice the regression of the observed monthly SSTs onto the 1910–2008 GW, AMO, IPO and IDV indices, respectively. Units are 0.5 K per standard deviation of the index

et al. 2007). The horizontal resolution is T106 and it uses 31 levels in the vertical.

To test the impact of the SSTs anomaly patterns we perform a set of SST-sensitivity experiments using the LMDZ model. The boundary conditions to force the model are defined as the 1910–2008 climatological monthly SSTs plus (minus) the global monthly associated GW, AMO or IPO anomaly patterns (Fig. 2) for the positive (negative) experiments. The impact of the IDV component was also tested. However, the results are not presented because this component is highly dependent on the AMO and IPO ones (Sect. 3.1).

Additional 12 experiments are performed to pin down the particular SST areas responsible for the impact of each component on West African rainfall. Therefore the SST anomaly patterns are restricted to certain oceanic regions. Table 2 summarizes the experiments and Fig. 3 depicts the areas used in the different experiments.

The simulations are run from April to October in ensemble mode with ten members. Each member differs

Table 2 Summary of the 15 experiments performed based on the HadISST1.1 and ERSSTv3 SST data sets

Name	Area of anomalous SSTs
GW experiments	
GW_all	World-wide
GW_T	Tropical (30S 30N)
GW_TA	Tropical Atlantic
GW_TI	Tropical Indian
GW_TP	Tropical Pacific
GW_TAI	Tropical Atlantic + Indian
IPO experiments	
IPO_all	World-wide
IPO_T	Tropical (30S 30N)
IPO_P	Pacific (55S 80N)
AMO experiments	
AMO_all	World-wide
AMO_T	Tropical (30S 30N)
AMO_A	Atlantic (55S 80N)
AMO_AM	Atlantic + Mediterranean
AMO_AMTIMC	Atlantic + Mediterranean + Tropical Indian + Maritime Continent
AMO_TIMC	Tropical Indian + Maritime Continent

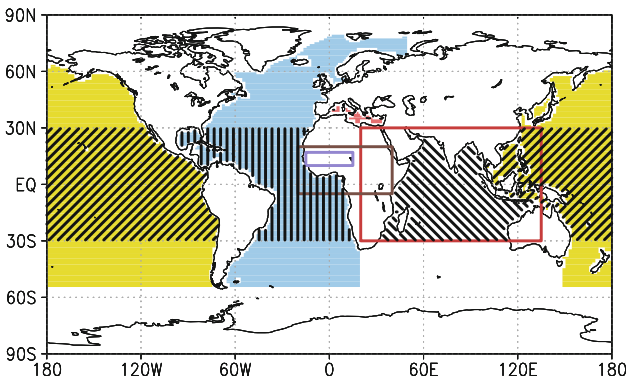

Fig. 3 Different areas used in the sensitivity experiments. Tropics (T) are hatched vertically for the Tropical Atlantic (TA), right tilted for the Tropical Pacific (TP) and left tilted for the Tropical Indian (TI) experiments. *Blue* is used to mark the Atlantic (A) area used in the AMO_A experiment. *Red* marks the area added as Mediterranean (M) to form the AMO_AM experiment. The *red box* indicates the Tropical Indian plus Maritime Continent area used in the AMO_TIMC experiment. Added to the Atlantic and Mediterranean areas (AM), they were used in the AMO_AMTIMC experiment. *Yellow* is used to mark the Pacific (P) area used in the IPO_P experiment. The figure also marks West Africa and Sahel areas with *brown* and *purple boxes*, respectively

only in the initial conditions. All the experiments are carried out for the HadISST1 and ERSSTv3 derived SST patterns. The greenhouse gases (GHG) are kept constant in time (CO_2 at 348 parts per million (ppm) and CH_4 at 1,650 ppm) and neither direct or indirect aerosol effects are included in the model. The experiments differ only in the SST forcing.

2.2.4 *Significance of results*

To test whether the response of the simulations differs we apply a two-sample *t* test for equal means assuming equal variances. The statistical significance of the correlations of unfiltered time series is based on a two-tailed *t* test. For filtered time series, the following Monte Carlo variant is applied: 1,000 pairs of random time series of the same length as the original one are low-frequency filtered using the same filter. The correlation between each pair is calculated to build a probability density distribution of correlations against which the original correlation is compared. The statistical significance of the spatial correlations is assessed using a two tailed *t* test with the effective degrees of freedom calculated as suggested by Bretherton et al. (1999). Correlation values are given throughout the text and tables indicating whether they are significant at the 95% (99%) level using one (two) asterisk.

3 Observed components of SST low-frequency variability and their relationship to Sahelian rainfall

3.1 Observed SST indices and patterns

The GW index shows a general increasing trend over the twentieth century (Fig. 1b). A weak negative trend (more prominent for the HadISST1 data set) is visible from the mid-1940s to 1970 in agreement to other studies (Hansen et al. 2006; Trenberth et al. 2007; Baines and Folland 2007). The 1945 uncorrected instrumental bias could be taking a part in this apparent cooling (Thompson et al. 2008). Coupled models forced with natural and anthropogenic factors show a certain mid-twentieth century cooling (Scott et al. 2000; Meehl et al. 2004; Hansen et al. 2005). Except for the beginning and the mid-1940s to 1970s cooling, our two GW indices are similar and show a high correlation (Table 1). According to results from coupled models, the GW index is primarily controlled by external forcing (Scott et al. 2000; Crowley 2000; Meehl et al. 2004). The main sources of the forcing are of natural origin before the 1970s (mainly solar), and of anthropogenic origin since then (Scott et al. 2000; Meehl et al. 2004; Barnett et al. 2005), principally driven by GHG emissions (Meehl et al. 2004).

Overall, the GW associated SST patterns show a worldwide warming, with the highest loadings over the tropical and southern Indian and Atlantic Oceans (Fig. 2a, e). There, the trends of approximately 1 K per century are in

the range of trends given by other authors for the twentieth century (Trenberth et al. 2007). Note that the patterns are not uniform and that there are areas of very small warming, like south of Greenland (more clear for the ERSSTv3 pattern). The lack of warming over this area is consistent with the response of coupled models to increased GHG (Meehl et al. 2007). Though the GW indices are very similar (Table 1), there are important differences between the associated SST patterns. This is in accordance with the differences in trends between different SST data sets already reported in other works (Vecchi et al. 2008; Falvey and Garreaud 2009). Overall, the ERSSTv3 data set shows world-wide warmer anomalies compared to the HadISST1 data set. The latter even shows a La Niña-like pattern with a modest cooling in the central and eastern equatorial Pacific basin (Vecchi et al. 2008). There are other important regional differences, like the one over the eastern equatorial Atlantic, where ERSSTv3 doubles HadISST1 anomalies. There are even bigger differences in the southern high latitudes, which could be connected to reduced data coverage over those regions.

The two AMO indices show a change from a negative to a positive phase in the mid-1920s, back to negative in the mid-1960s, and, finally, back to positive in the mid-1990s (Fig. 1b). These results are coherent with other studies on the AMO using EOF analysis, either on world-wide or on North Atlantic SSTs (Cai and Whetton 2001; Baines and Folland 2007; Polyakov et al. 2009), and also using averages over the North Atlantic (Ting et al. 2009; Hodson et al. 2009; Trenberth and Shea 2006; Zhang and Delworth 2006; Sutton and Hodson 2005; Knight et al. 2005; Knight 2009). The indices derived from both data sets are similar and show a high correlation (Table 1). The time period chosen for this study spans approximately a cycle and a half of the AMO.

The associated global AMO patterns (Fig. 2b, f) show an inter-hemispheric dipole with warm SSTs in the North Atlantic and cold ones in the South Atlantic, in accordance with other works (Knight et al. 2005; Sutton and Hodson 2005; Trenberth and Shea 2006; Hodson et al. 2009). There are warm anomalies over the North Pacific and mostly cold anomalies over the Indian Ocean. The former are suggested to be physically related to AMO through ocean–atmosphere fluxes (Dima and Lohmann 2007). There are positive loads over the Mediterranean Sea. The AMO patterns obtained from both data sets differ, though less than for the GW case (Table 3). The different horizontal resolution of the data sets (1° for HadISST1.1 and 2° for ERSSTv3) could explain part of the small scale differences, mainly over coastal regions. The reduced coverage over the southern Indian Ocean could also matter in the different magnitude of the anomalies between data sets over this region.

The two IPO indices (Fig. 1b) show alternating positive and negative phases with four main changes of regime: in the mid 1920s, mid 1940s, late 1970s (the 1976/1977 "climate shift" of Miller et al. 1994) and late 1990s. The indices are in agreement with other works on the IPO and on the Pacific Decadal Oscillation (Power et al. 1999; Mantua and Hare 2002; Meehl et al. 2009). The IPO indices derived from both SST data sets show agreement, though their correlation is lower than for the GW and AMO cases (Table 1). The main differences are at the beginning of the time series, when data was scarcer over the Pacific basin. The work of Meehl et al. (2009) suggests that forced and internal variability contribute to the IPO behaviour.

The two IPO associated SST patterns (Fig. 2c, g) show a cooling in the extra-tropical Pacific, most noticeably over the North Pacific, and a warming in the tropical eastern sector, in agreement with other works (Power et al. 1999; Mantua and Hare 2002; Meehl et al. 2009). Outside the Pacific, they show a warming over the tropical Atlantic (also in agreement with Meehl and Hu 2006). However, they disagree on the actual regions and magnitude. There are also positive loadings over the Indian Ocean, in agreement with studies that suggest that the IPO affects this basin (Cole et al. 2000; Crueger et al. 2009).

The IDV indices show alternation between positive and negative phases (Fig. 1b). The indices derived from both data sets are similar and show a high correlation (Table 1). They show oscillations with smaller amplitude and period at the beginning of the time series. However, since the mid 1940s, only two regimes are observed, one in negative phase (until 1970) and the other one in positive phase (since 1970). Note that while the correlations between the AMO and the IPO indices are weak, the IDV shows high correlations with the AMO and the IPO (Table 1).

In turn, the IDV associated patterns show a warming over the whole Indian basin, with the highest loads in the south mid-latitudes (Fig. 2d, h). These global patterns show great resemblance (with a change of sign) with the inter-hemispheric pattern (Fig. 1c; Table 3). The inter-hemispheric pattern was obtained from the regression of the observed SSTs onto the low-frequency (using a 13-year running mean) rainfall over Sahel. Note that in Fig. 1c HadISST1 data set is used, and that a similar result is obtained with ERSSTv3 data set (not shown).

As the inter-hemispheric pattern, the IDV shows loadings over other basins that are similar to the negative phase of the AMO in the Atlantic and the positive one of the IPO in the Pacific (Fig. 2; Table 3). This suggests that at least some part of the IDV is co-varying with the AMO and the IPO. To test to what extent the IDV is independent from the AMO and the IPO, we recalculated this index following the same procedure as explained in Sect. 2.2.1 but using a different SST data set. Instead of using the residual SST to

Table 3 Spatial correlations (between 60°S and 60°N) between the GW, AMO, IPO, IDV and the inter-hemispheric patterns

	GW	AMO	IPO	IDV	inter-hemispheric
GW	0.507*	-0.203	0.218	0.207	-0.387
AMO	-0.295	0.697**	-0.436	-0.756**	0.872**
IPO	0.194	-0.190	0.613*	0.670**	-0.692**
IDV	0.467	-0.831**	0.578*	0.703**	-0.921**
inter-hemispheric	-0.520*	0.849**	-0.597*	-0.968**	0.713**

Upper triangle (light shading) shows the correlation for the patterns derived from the ERSSTv3 data set; lower triangle (dark shading) shows the correlation for the patterns derived from the HadISST1 data set; the diagonal shows the correlation between the ERSSTv3 and HadISST1 derived patterns. One (two) asterisk indicates 95% (99%) significant correlations

calculate the first EOF in the Indian basin, we reconstructed this data using only the information contained in the AMO and the IPO signals. As a consequence, we first regressed the residual SSTs onto the AMO and the IPO indices to obtain two patterns. With these two patterns and the time series of the AMO and the IPO indices we performed the reconstruction. Though not correct (AMO and IPO signals do not form part of a basis set to describe the SST field because they are obtained from EOF analysis applied to different regions), we use this reconstructed SST to estimate to what extent the IDV index and pattern could be obtained from the AMO and the IPO. Figure 4 shows the original and reconstructed IDV indices, which are the principal component associated with the first EOF of the residual and reconstructed SST over the Indian basin. The original and reconstructed IDV indices are very similar, especially for the HadISST1 data set. Figure 4 also shows the world-wide regression of the original and reconstructed SSTs onto the original and reconstructed IDV indices, respectively. Despite some differences, especially for the ERSSTv3 data set in the North Atlantic, the overall reconstructed pattern is quite similar to the original one. The world-wide (60S–60N) spatial correlations between original and reconstructed patterns are higher (0.84** and 0.85** for ERSSTv3 and HadISST1, respectively) than between the ERSSTv3 and the HadISST1 original patterns (Table 3). This indicates that most of the IDV is implicitly included in the global AMO and IPO signals.

A possible explanation is that the AMO and the IPO do have a physical impact on decadal variability over the Indian Ocean. This is supported by the works of Cole et al. (2000) and Crueger et al. (2009) that show signals of the IPO on corals in the Indian basin. Experiments with coupled models in which the Atlantic thermohaline circulation has been altered show impacts on the Indian basin (Lu and Dong 2008). In addition, the data coverage over this basin could lead to an under-representation of its variability. Before 1960 there was approximately 60% data coverage over the South Indian Ocean. Conversely, it reached approximately 90% over the North Atlantic and the eastern North Pacific, where the main loads of the AMO and the IPO lie. This difference in coverage jointly with the reconstruction technique, based on global EOFs, could lead to an enhancement of the link between the AMO and the IPO signals and the IDV one.

The AMO and the IPO are two well documented and highly independent oscillations that are related, at least in part, to a physical phenomenon (Knight et al. 2005; Meehl and Hu 2006). Nevertheless, the IDV, like the inter-hemispheric pattern (Folland et al. 1986), is a statistical construction with no relationship, to our knowledge, to internal variability of SSTs in the Indian Ocean basin. The IDV component has been shown to be highly dependent on the AMO and the IPO. As a consequence, only the GW, the AMO and the IPO modes will be considered to study the relationship between the low-frequency variability of Sahel rainfall and SSTs.

3.2 Relationship with observed Sahel rainfall variability

The SST indices show a marked connection with summer precipitation over West Africa. The 1910–2002 regression of the CRUTS2.1 observed precipitation onto the GW index (Fig. 5c) shows a zonally elongated drying over the Sahel and an increase in precipitation over western equatorial Africa. There are areas of intense drying over the western Sahel and Ethiopia. The pattern is similar for the second half of the twentieth century (Fig. 5f). The second most intense area of drying appears over Chad.

Figure 5d shows the regression pattern of the CRUTS2.1 observed rainfall onto the 1910–2002 AMO index. Increased rainfall over the Sahel is related to the positive phase of the AMO in accordance with previous studies (Folland et al. 1986; Rowell et al. 1995; Zhang and Delworth 2006; Knight et al. 2006; Ting et al. 2009). Figure 5g shows a similar pattern for the period from 1957 to 1998, even though it only spans half of the AMO cycle.

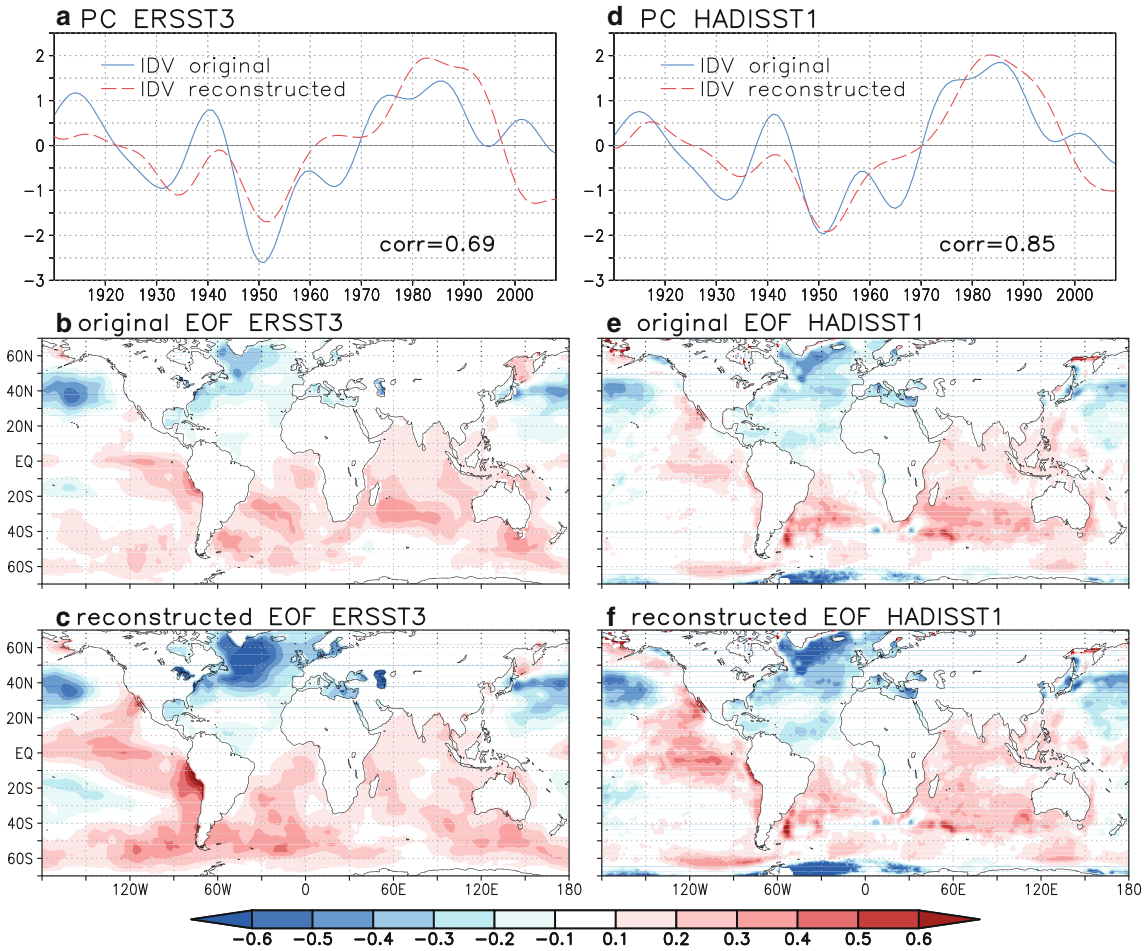

Fig. 4 Indian decadal variability from original and reconstructed data: **a** the standardized IDV original index (*solid blue*) and the IDV index obtained from the AMO and the IPO reconstructed data (see details in the text) using ERSSTv3 data set; **b** regression of the low-frequency filtered residual (after removal of the GW signal) SSTs from ERSSTv3 data set onto the IDV original index; **c** regression of the SSTs reconstructed from the AMO and IPO indices and associated patterns (see details in the text) onto the IDV reconstructed index. **d**–**f** the same as **a**–**c** but using HadISST1 data set. Units for the regressions are K per standard deviation

Sahel rainfall shows a stronger statistical connection to the AMO than to the GW. This is in accordance with higher correlations between the low-frequency Sahelian rainfall and the AMO indices (Table 4).

The observed precipitation over the Sahel shows a significant negative relationship with the IPO index over the whole and late twentieth century (Fig. 5e, h). It relates the positive phase of the IPO to a decrease in Sahel rainfall, in accordance with Joly (2008). The main loadings are located over the Sahelian western coast, Chad and Ethiopia. Though both lead to a similar pattern of drought, the relationship between Sahel rainfall and the IPO is stronger than with the GW (Fig. 5; Table 4).

As a summary, the positive phases of the GW and the IPO and the negative phase of the AMO are statistically related to decreased rainfall over the Sahel.

4 Simulation results

4.1 Model performance based on AMIP-like experiments

We use the ensemble mean of the LMDZ simulations forced only by the observed SST record from 1957 to 1998. Over West Africa the model reproduces a reasonable summer precipitation climatology, albeit with smaller meridional extension (Fig. 5b). The northern boundary of the Sahel is approximately simulated 2° southward with respect to the observations.

The model is capable of reproducing the decreasing precipitation trend over the Sahel in the last part of the twentieth century (Fig. 1a). Its behaviour is comparable to the one shown by other state-of-the-art models. For

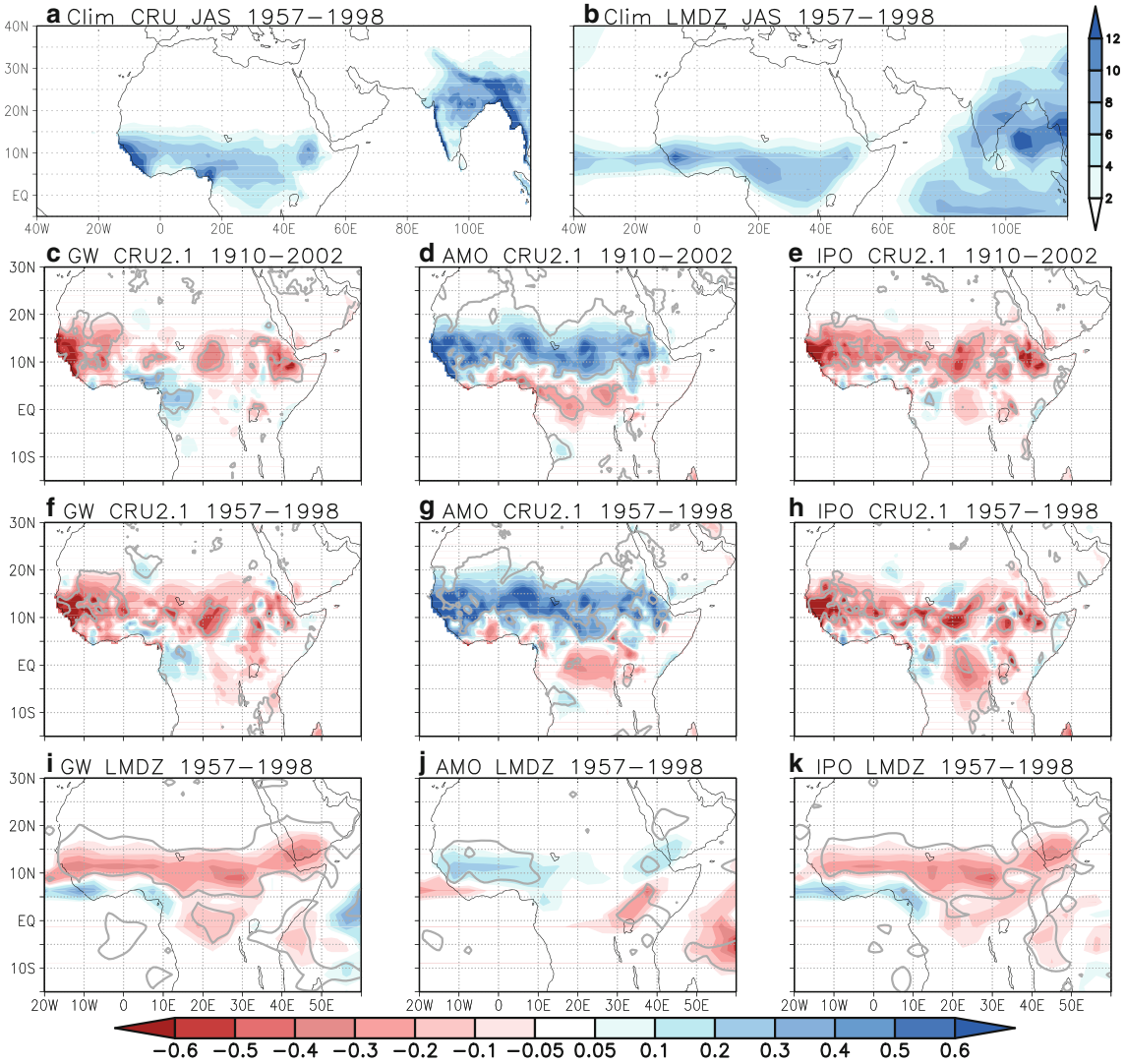

Fig. 5 Climatology of summer (July–September) rainfall (in mm/day) for CRUTS2.1 data **(a)** and LMDZ model **(b)** between 1957 and 1998. Regression of CRUTS2.1 summer precipitation onto the 1910–2002 **c** GW, **d** AMO and **e** IPO indices derived from ERSSTv3 data set. Regression of CRUTS2.1 summer precipitation onto the 1957–1998 indices: **f**–**h**. Regression of LMDZ summer precipitation onto the 1957–1998 indices: **i**–**k**. Each index was standardized for each period. *Grey contour* marks 95% significant regions (according to a *t* test). Units for the regressions are mm/day per standard deviation of the index

Table 4 Correlations between the low-frequency variability of Sahel rainfall (using a 13-year running mean) and the GW, AMO and IPO indices

	ERSSTv3	HadISST1
GW	−0.48	−0.42
AMO	0.78**	0.86**
IPO	−0.55*	−0.57*

One (two) asterisk indicates 95% (99%) significant correlations

comparison, Fig. 1a presents the low-frequency variability for the ECHAM5 model. Both models underestimate the magnitude of the drought by a factor of approximately 2/3. This underestimation of the trend by models is mentioned in other studies (Sutton and Hodson 2005; Zhang and Delworth 2006; Tippet and Giannini 2006; Zhou et al. 2008). Ensemble averaging could explain part of the underestimation because it reduces the variability. Other factors, like errors in land-surface feedback representation and the absence of dynamic vegetation could also contribute to it (e.g. Zeng et al. 1999; Giannini et al. 2003; Koster et al. 2004).

The correlation between the low-frequency filtered summer (July–September) precipitation from CRUTS2.1 and the LMDZ and ECHAM5 models is 0.89** and 0.97**, respectively. Figure 1a shows the observed partial recovery from the dry conditions in the 1980s to a less dry state in the 1990s. Driven only by varying monthly SSTs,

the models simulate a beginning of recovery at the end of the simulations, although a longer run would be necessary to fully assess this fact.

Figures 5i–k show the regression of the simulated ensemble mean precipitation onto the GW, the AMO and the IPO indices. Similarly to the observations, the model shows a zonally elongated drying over the Sahel associated with a rising GW index (Fig. 5i). The dry belt is narrower than in the observations, in agreement with a narrower Sahel shown by the model's climatology (Fig. 5b). A precipitation increase over the Sahel, mainly west of 10E, and a drying over southern Ethiopia and Sudan is associated with the positive phase of the AMO (Fig. 5j). Simulated Sahelian drying is associated with an increasing IPO index (Fig. 5k). The main loads are south of 15N, in accordance with the observations. The magnitudes of the regression patterns are underestimated by the model, especially for the AMO component.

The LMDZ model reproduces the observed low-frequency variability of Sahelian precipitation and the observed link between West African rainfall and the GW, AMO and IPO indices when forced by observed global historical SSTs.

4.2 Idealized experiments

4.2.1 GW simulations

Figures 6 and 7 show the results obtained for the GW experiments with ERSSTv3 and HadISST1 data sets, respectively. The GW_all experiments show a drying over the Sahel and an increase of precipitation over the Guinea Gulf (Figs. 6a, 7a). They show increased subsidence over West Africa, with anomalous divergence in low levels (850 hPa) (Figs. 6a, 7a) and the opposite in high levels (not shown). The monsoon is weakened and its northern limit and the Intertropical Convergence Zone (ITCZ) are shifted southwards (not shown). Simulated West African rainfall anomalies in the HadISST1 SST forced GW experiment are weaker compared to the integration driven by the ERSSTv3 GW SSTs. This is consistent with the overall weaker SST anomalies for the HadISST1 data set (Fig. 2e). The simulated precipitation response is approximately 17% weaker over the Sahel (defined hereafter as the area between 15W–15E and 10N–17N, Fig. 3) and 15% in the Gulf of Guinea (defined as the area between 15W–15E and 0N–8N). This latter is in agreement with the weaker SST trend in the Eastern Tropical Atlantic in the HadISST1 data set.

The tropical part of the GW signal controls the anomalies of circulation and precipitation over West Africa. The GW_T experiments (Figs. 6b, 7b) reproduce most of the anomalous rainfall simulated in the GW_all experiments. The spatial correlations of the precipitation response over West Africa (hereafter defined as the area between 20W–40E and 5S–20N, Fig. 3) between the GW_all and the GW_T simulations are above 0.9**. The GW_T integrations reproduce the simulated subsidence over West Africa (Figs. 6b, 7b), the weakening of the monsoon and the southward displacement of the ITCZ (not shown). The simulated drying over the Sahel is larger in the GW_T experiments than in the GW_all integrations (between 20 and 30% over the Sahel, depending on the data set). This suggests that the warming of the extra-tropics is partially counteracting the effect of the tropics.

Warm anomalies over the tropical Atlantic basin increase low level convergence (see experiment GW_TA in Figs. 6c, 7c) and high level divergence (not shown) over this ocean basin. They induce a reduction of the monsoon westerlies and are responsible for the increase in rainfall over this ocean basin and over the Gulf of Guinea. This oceanic and coastal precipitation increase is partially counteracted by the warming in the Indian and Pacific ocean basins (Figs. 6d, e, 7d, e).

The Sahelian precipitation decrease is mainly controlled by the warming of the tropical Indian and Pacific ocean basins (Figs. 6d, e, 7d, e). This is in agreement with the results of Giannini et al. (2003), Bader and Latif (2003), Lu and Delworth (2005), Hagos and Cook (2008) and Caminade and Terray (2009). The warming of the tropical Indian Ocean induces subsidence over the western part of West Africa, with low level divergence (Figs. 6d, 7d) and high level convergence (not shown). The Indian Ocean warming accounts for roughly 40–50% of the Sahelian drying. The SST anomalies over the tropical Pacific Ocean reduce rainfall mainly in the eastern Sahel through low level divergence (Figs. 6e, 7e). The role of the tropical Indian Ocean warming in reducing rainfall over the west Sahel and the tropical Pacific Ocean warming over the east is consistent with the results of Bader and Latif (2003).

At the first order, West African precipitation responds linearly to the forcing of the individual tropical ocean basins. The summation of the West African rainfall response in the different tropical ocean basin experiments is close to the full tropical ocean experiment (not shown). The spatial correlation coefficient between the precipitation anomalies from the GW_T experiment over West Africa and the sum of the GW_TA + GW_TI + GW_TP experiments is 0.94** (0.81**) for the ERSSTv3 (HadISST1) data set.

The combined SST forcing of the tropical Atlantic and Indian Oceans (GW_TAI) reproduces most of the anomalous West African precipitation associated with the GW pattern (Figs. 6f, 7f). The spatial correlation coefficient between the West African precipitation response in the GW_TAI experiment and in the GW_T simulation is

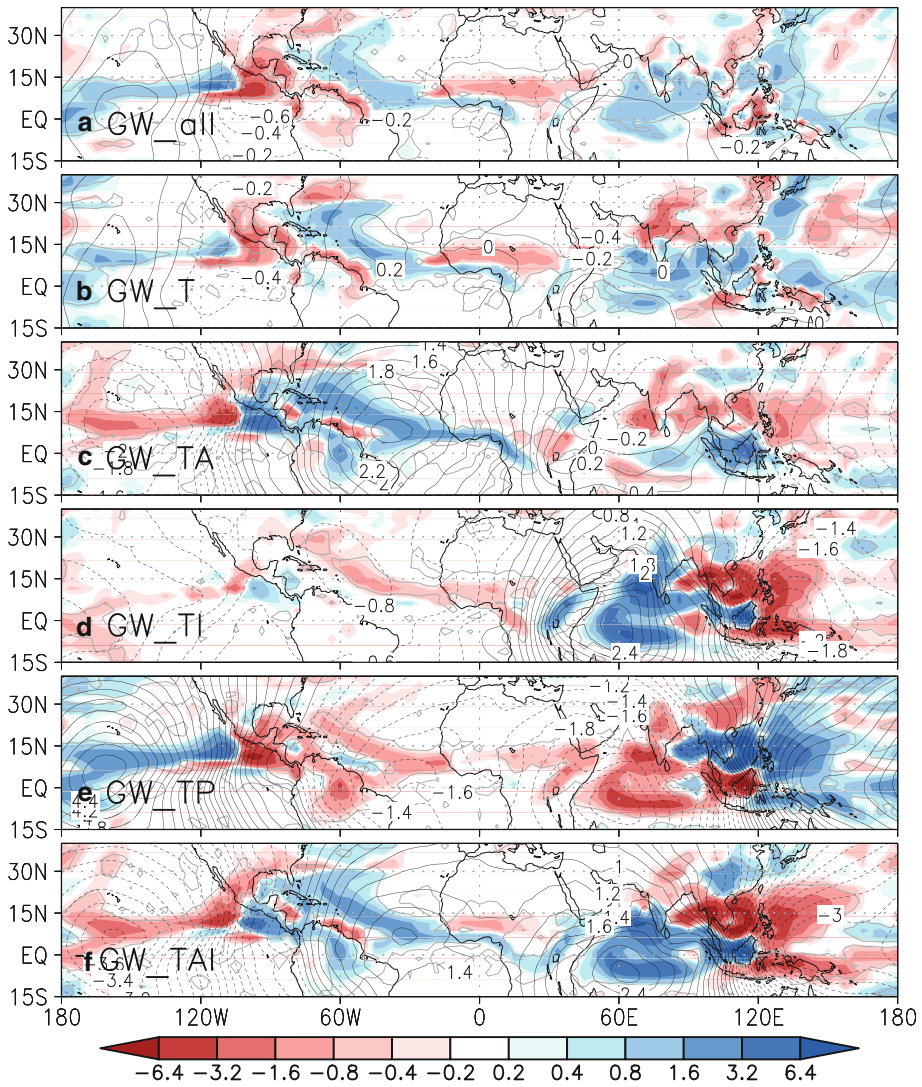

Fig. 6 Results for the GW experiments. Differences in July–September precipitation (mm/day) between the positive minus negative experiments with ERSSTv3 data set using: **a** global (GW_all), **b** tropical (GW_T), **c** tropical Atlantic (GW_TA), **d** tropical Indian (GW_TI), **e** tropical Pacific (GW_TP) and **f** tropical Atlantic plus tropical Indian (GW_TAI) SST anomalies. *Grey contour* marks 95% significant regions (according to a *t* test). Anomalies of velocity potential (10^6 m^2/s) at 850 hPa are also shown in contours. *Dashed lines* mark negative anomalies. Interval for the contour is 0.2×10^6 m^2/s

0.77** (0.76**) when forced with the ERSSTv3 (HadISST1) SST data set. The response is similar to the addition of the effects of the tropical Atlantic (GW_TA) and tropical Indian (GW_TI) experiments (not shown), which again suggests linearity in the response to the tropical warming. The rainfall response due to the SST anomalies of the tropical Indian and Atlantic oceans explains around 60–65% of the drought over the Sahel. The remaining 30–35% of precipitation anomalies is forced by the tropical Pacific basin.

In summary, the warming of the tropical Pacific and Indian Oceans related to GW weakens the monsoon and decreases Sahelian rainfall due to enhanced subsidence over West Africa. The tropical Atlantic warming is associated with a southward shift of the monsoon and increased rainfall over the Gulf of Guinea.

4.2.2 AMO simulations

A precipitation increase over the Sahel and a slight decrease along the Gulf of Guinea coast and Ethiopia is simulated by the AMO_all experiments (Figs. 8a, 9a). The ITCZ shifts northwards (not shown). The model shows a nearly 20% higher rainfall increase over the Sahel when forced by the HadISST1 AMO_all SST pattern compared to the equivalent ERSSTv3 SST pattern. The tropical part of the AMO pattern controls the overall tropical structure of the circulation and the precipitation anomalies (Figs. 8b, 9b), but is not able to account for the West African rainfall anomalies simulated in the full AMO experiment, neither for the northward shift of the ITCZ (not shown). This suggests that an important part of the AMO impact over West Africa comes from the extra-tropics.

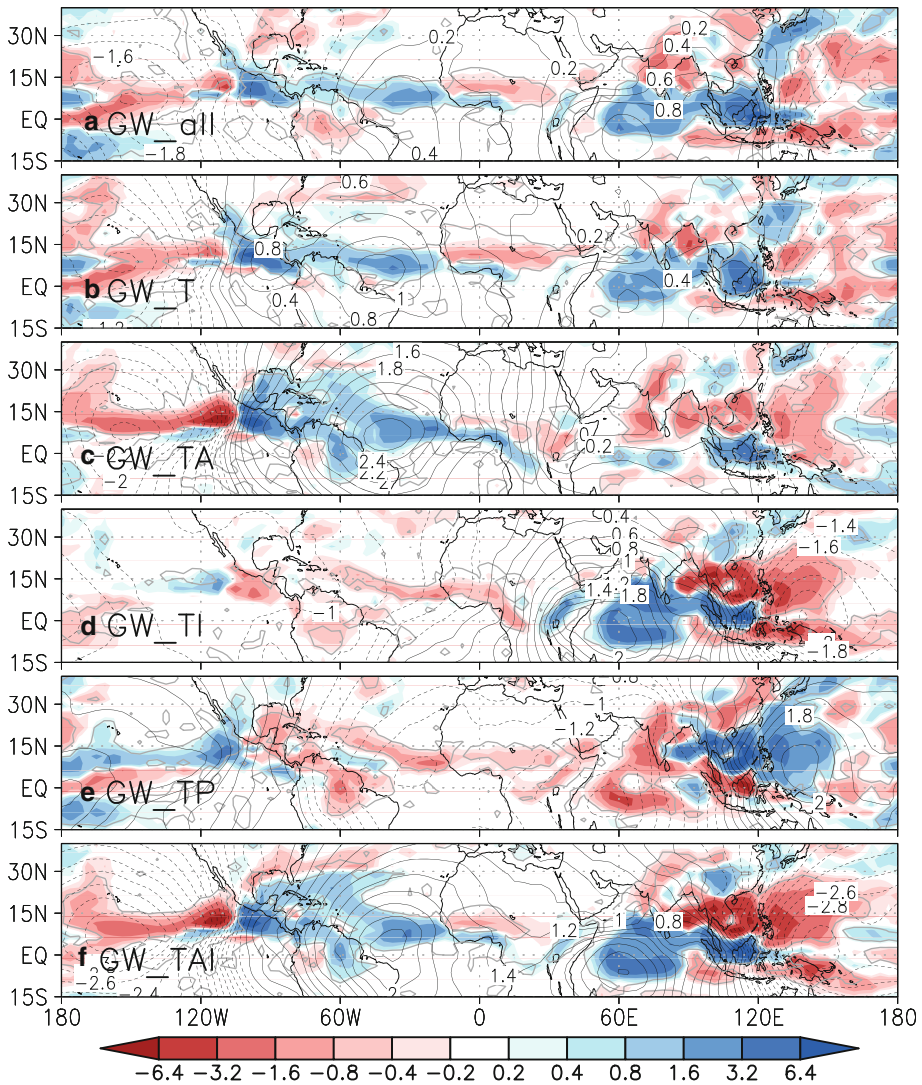

Fig. 7 Same as Fig. 6 but for the HadISST1 data set

The AMO_A experiments show that the contribution of the Atlantic can account for rainfall anomalies over this basin (Figs. 8c, 9c). Over West Africa they show a pattern that resembles the AMO_all (with a spatial correlation of 0.74** and 0.57 for ERSSTv3 and HadISST1 data sets, respectively), but the anomalies of rainfall over the Sahel are weak and even non-significant for the ERSSTv3 data set. This is in agreement with other works that only considered the Atlantic part of the AMO (Sutton and Hodson 2005; Hodson et al. 2009). Other regions, aside from the Atlantic basin, are important in establishing the AMO impact on West Africa.

The AMO SST patterns show a positive anomaly over the Mediterranean Sea (Fig. 2b, f). Warm anomalies in this region are related to positive precipitation anomalies over the Sahel through enhanced moisture advection (Rowell 2003; Jung et al. 2006; Fontaine et al. 2009). Therefore, we repeated the AMO experiment restricting the anomalies to the Atlantic and Mediterranean basins. The inclusion of the Mediterranean Sea increases the low level convergence over the Atlantic basin and the western part of West Africa (Figs. 8d, 9d). The AMO_AM experiments simulate a northward shift of the ITCZ (not shown). They show a higher resemblance with the precipitation patterns of the AMO_all experiments (spatial correlation over West Africa of 0.80** and 0.86** for ERSSTv3 and HadISST1 experiments) and an increased rainfall response over the Sahel for the ERSSTv3 experiment. Nevertheless, the two oceanic regions account only for 60% of the AMO induced Sahelian rainfall anomalies and show only a weak impact over the eastern Sahel.

A prominent feature of the AMO_all experiments is the precipitation decrease and the enhancement of high level divergence (not shown) over the Indian Ocean, east of Africa. The AMO_TIMC simulations, performed with the AMO anomalous SST pattern restricted to the tropical Indian and Maritime Continent region (red box in Fig. 3), confirm that these features are locally connected to the

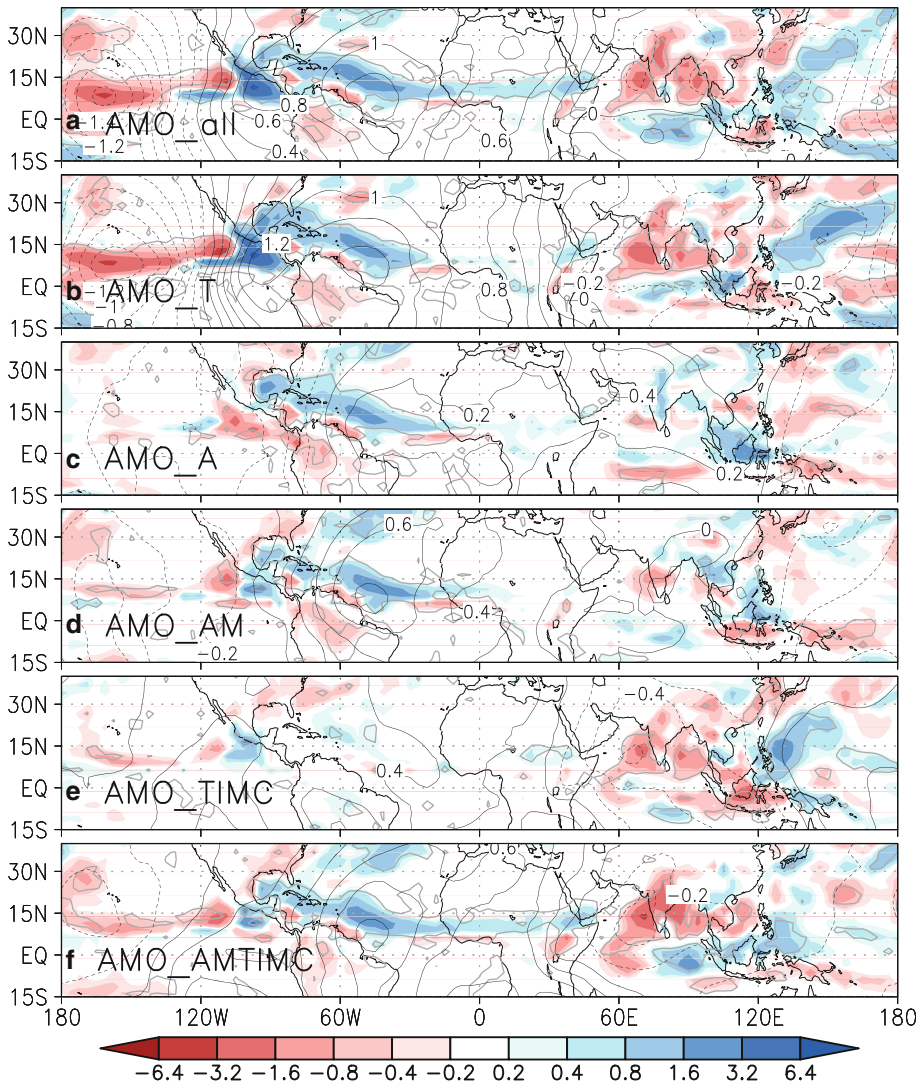

Fig. 8 Results for the AMO experiments. Differences in July–September precipitation (mm/day) between the positive minus negative experiments with ERSSTv3 data set using: **a** global (AMO_all), **b** tropical (AMO_T), **c** whole Atlantic (AMO_A), **d** whole Atlantic plus Mediterranean (AMO_AM), **e** tropical Indian and Maritime Continent (AMO_TIMC), **f** whole Atlantic plus Mediterranean, tropical Indian and Maritime Continent (AMO_AMTIMC) SST anomalies. *Grey contour* marks 95% significant regions (according to a *t* test). Anomalies of velocity potential (10^6 m^2/s) at 850 hPa are also shown in contours. *Dashed lines* mark negative anomalies. Interval for the contour is 0.2×10^6 m^2/s

negative SST anomalies in this basin (Figs. 8e, 9e). These weak SST anomalies have little impact over West Africa (Figs. 8e, 9e). When combined with the Atlantic and Mediterranean SSTs they enhance low level convergence (Figs. 8f, 9f) and high level divergence (not shown) over West Africa. They amplify the Sahelian rainfall anomalies. The AMO_AMTIMC experiments account for 85 and 140% of the Sahel precipitation anomalies in the AMO_all experiments using the ERSSTv3 and the HadISST1 data set, respectively. They are able to reproduce the West African precipitation anomaly patterns (Figs. 8f, 9f), with spatial correlations of 0.9** between the AMO_all and AMO_AMTIMC experiments. Note that the Maritime Continent can have a notable effect on the global atmospheric circulation. Even though the SST anomalies over this region are weak (Fig. 2), they have to be taken into account to retrieve most of the original AMO_all pattern over West Africa, especially for the HadISST1 data set (not shown).

In summary, the AMO impacts West Africa through a northward displacement of the ITCZ and leads to a rainfall enhancement (decrease) over the Sahel (Guinea Gulf). Though the Atlantic and Mediterranean anomalies drive most of the West African rainfall pattern, the Indian basin (including the Maritime Continent) amplifies the rainfall anomalies.

4.2.3 IPO simulations

The IPO_all experiments show a reduction of rainfall over the Sahel (Figs. 10a, 11a). It is connected to upper level convergence over West Africa (not shown). The negative anomalies extend into northern Ethiopia and south-eastern Arabia. The model shows 40% higher anomalies over the Sahel when forced with the IPO pattern based on the HadISST1 data set.

The tropical rainfall and circulation in the IPO_all experiments is controlled by the tropical part of the SST

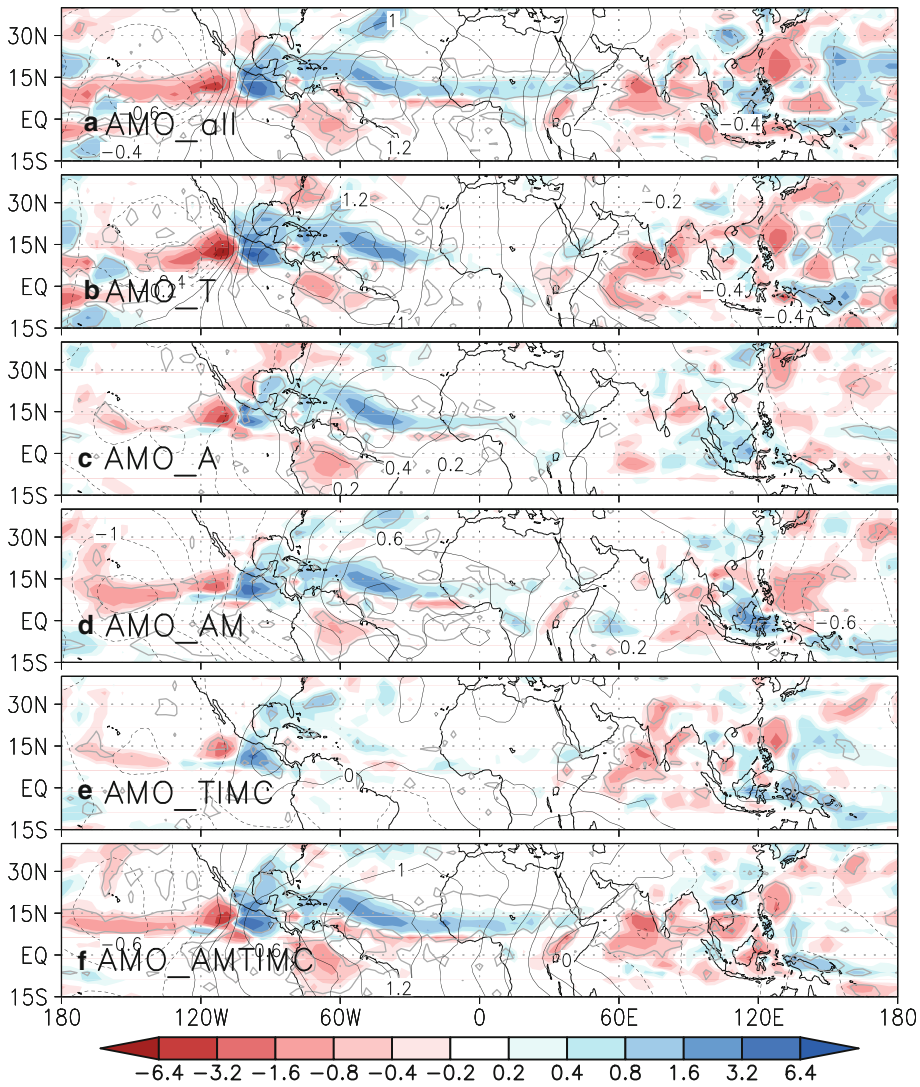

Fig. 9 Same as Fig. 8 but for the HadISST1 data set

anomalies (Figs. 10b, 11b). The IPO_T forcing accounts for approximately 70% of the Sahelian precipitation anomalies induced by the IPO SST pattern.

The Pacific region of the IPO SST pattern controls the precipitation anomalies over the Pacific, the Caribbean and over northern South America. The north African impact is restricted to drying over northern Ethiopia and along the Guinea Coast (Figs. 10c, 11c). The IPO_P simulations show a significant precipitation reduction over the western Indian Ocean. It is associated with an increase of the anomalous low (high) level divergence (convergence) that is not obtained in the IPO_all experiment. The SSTs over the Indian Ocean basin seem to be crucial for the overall precipitation pattern over West Africa.

In summary, the IPO pattern reduces rainfall over the Sahel through enhanced subsidence over West Africa. The experiments suggest that the whole tropical pattern, and not only the Pacific part, is responsible for the effect.

5 Sahel drought and partial recovery

In the 1980s the Sahel suffered from an extreme drought. Since the end of the 1980s there is some recovery toward climatology. We defined three periods: the wet period over the Sahel from 1957 to 1965, the dry period from 1980 to 1990 and the recovery period from 1995 to 2002.

Three unfavourable SST conditions coincided during the 1980s drought: a positive GW trend, a negative phase of the AMO and a positive phase of the IPO (Fig. 1b). To estimate the relative impact of each ocean pattern on the SST driven drying trend we first used the 1910–2002 observed regression plots in Fig. 5. Each regression map (Fig. 5c–e) was multiplied by the change in the corresponding index (in standard units) from the wet period to the dry period. The three weighted regression maps were summed up to form the drought map (Fig. 12b). This drought map was compared with the observed rainfall

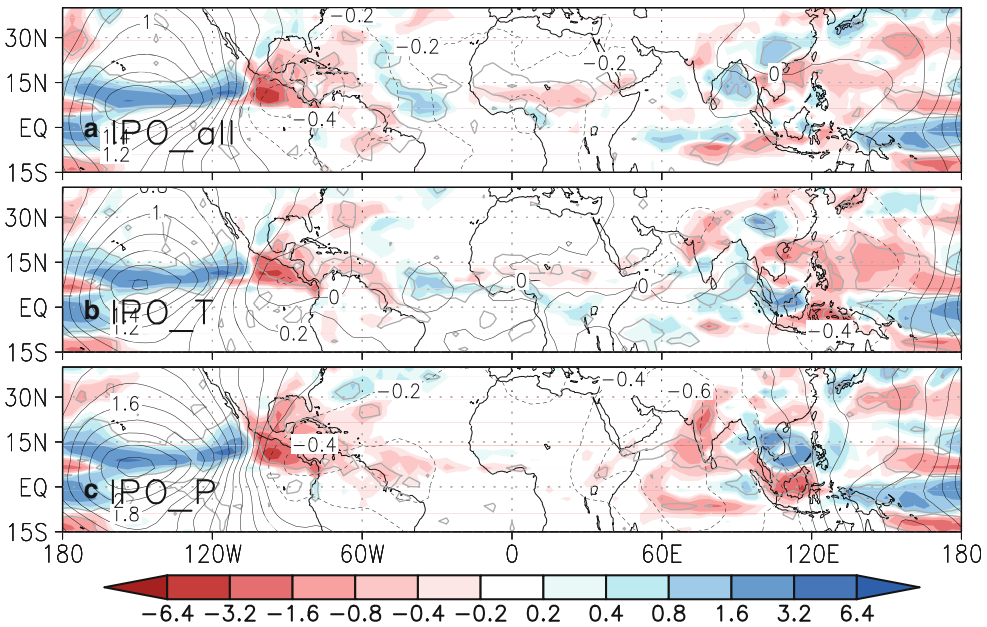

Fig. 10 Results for the IPO experiments. Differences in July–September precipitation (mm/day) between the positive minus negative experiments with ERSSTv3 data set using: **a** global (IPO_all), **b** tropical (IPO_T) and **c** whole Pacific (IPO_P) SST anomalies. *Grey contour* marks 95% significant regions (according to a *t* test). Anomalies of velocity potential (10^6 m^2/s) at 850 hPa are also shown in contours. *Dashed lines* mark negative anomalies. Interval for the contour is 0.2×10^6 m^2/s

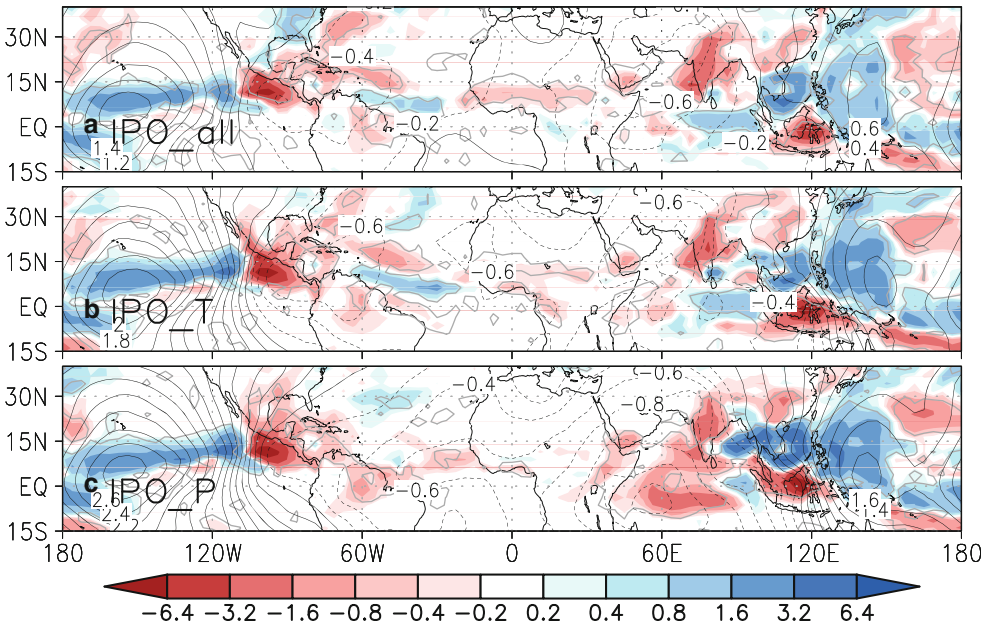

Fig. 11 Same as Fig. 10 but for the HadISST1 data set

change from the wet to the dry period (Fig. 12a). The two precipitation patterns are similar over West Africa with a spatial correlation of 0.89**. The 'regressed' Sahel drought was approximately 25% smaller than the observed rainfall decline. Using the drought map as reference 10% of the 1980s drought was caused by the GW, 50% by the AMO and 40% by the IPO.

The partial recovery of Sahel rainfall can be understood as a competition between the decrease in precipitation due to the increased GW and the enhancement of precipitation due to the mid-1990s change of phase of the AMO and the IPO (Fig. 1b).

We have applied the same analysis for the recovery period from 1980–1990 to 1995–2002. The obtained recovery map overestimates the rainfall increase, especially over the western Sahel (Fig. 12d). The spatial correlation between the recovery map and the observed rainfall increase pattern over West Africa (Fig. 12c) is 0.65*. The AMO was the main driver of the rainfall recovery over West Africa (+80%), counteracted by the GW (−20%).

An equivalent calculation taking into account the simulation results also highlights the role of the AMO signal in driving Sahel's drought and its partial recovery (not shown).

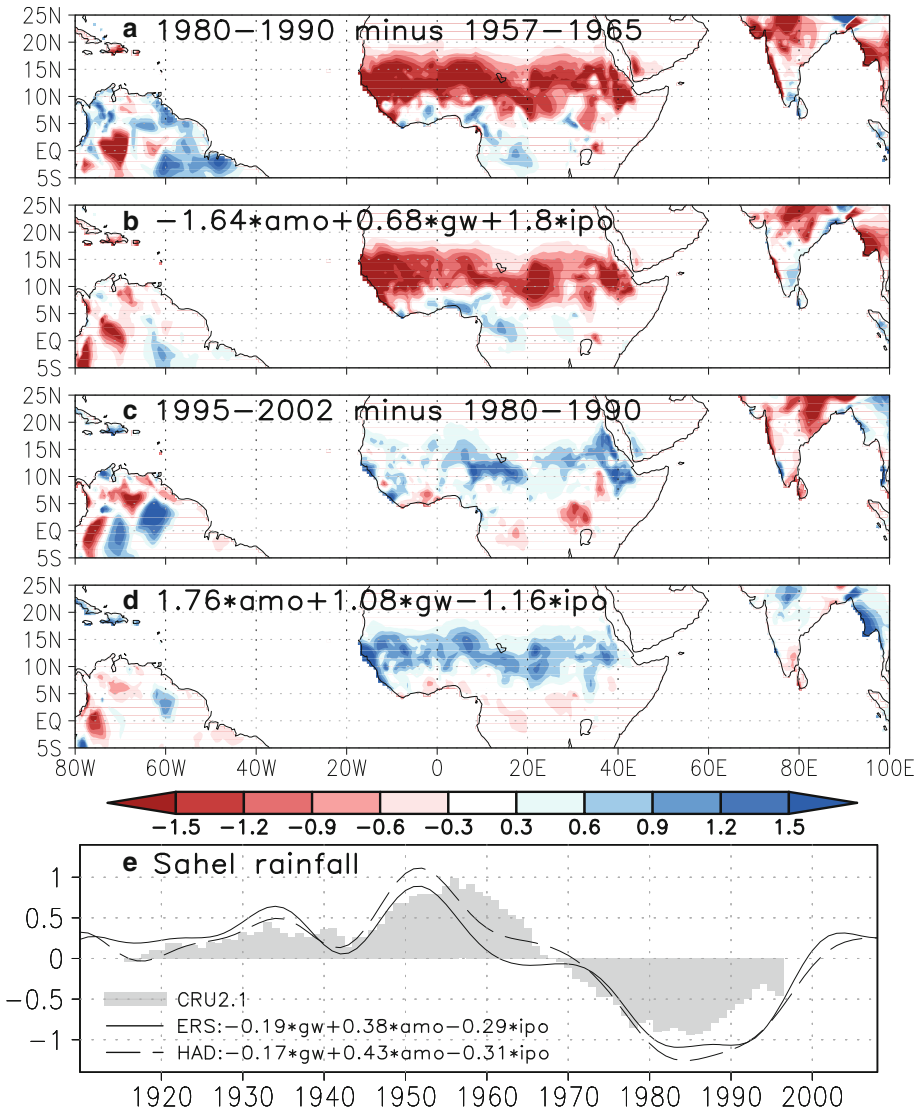

Fig. 12 Observed drought and partial recovery: **a** difference of climatologies between observed precipitation in the 1980s and the period 1957–1965; **b** drought of Sahel rainfall estimated from the weighted addition of the regression of observed precipitation onto GW, AMO and IPO indices (see details in the text); **c** difference of climatologies between observed precipitation in the 1995–2000 period and the 1980s; **d** partial recovery of Sahel rainfall estimated from the weighted addition of the regression of observed precipitation onto GW, AMO and IPO indices (see details in the text). **e** Low-frequency evolution of Sahel precipitation: low-frequency observed (13-year running mean) in *grey bars*, and estimated from the addition of the weighted GW, AMO and IPO ERSSTv3 (HadISST1) indices in *solid (dashed) black line* (see text for details in the weighting). Units are mm/day

The GW, the AMO and the IPO may help to reconstruct the decadal Sahelian rainfall variability. Figure 12e shows the reconstructed rainfall using the GW, AMO and IPO indices and the observed decadal Sahelian rainfall. For this reconstructed rainfall index we added up the weighted GW, AMO and IPO indices. To obtain the weights we used the regression plots of observed West African rainfall onto each index (Fig. 5c–e). The weights were calculated as the average over the Sahel region of these regression plots. The reconstructed rainfall is a good estimate for the observed precipitation (correlation is 0.89**/0.94** using ERSSTv3/HadISST1).

Given this high correlation, the regression of the observed SST onto the reconstructed index (not shown) yields a pattern very similar to the inter-hemispheric pattern (Fig. 1c) (global spatial correlations of 0.96**/0.98** for ERSSTv3/HadISST1 data set). This suggests that the inter-hemispheric pattern (Folland et al. 1986) can be understood as the weighted addition of the GW, AMO and IPO patterns.

6 Limitations and discussion

There are several limitations to this study that must be commented.

Regarding the methodology, our analysis of the SST components is based on filtered time series, so one could wonder how dependent the results are on the choice of the cut-off frequency. For instance, the decadal components AMO, IPO and IDV are based on the residual SST after subtraction of the GW signal, so any change of the cut-off frequency in the definition of GW could alter not only GW index, but also all the others. To have an estimation, we recalculated all indices and patterns but using 20 year cut-off frequency instead of 40 year for the definition of GW.

This choice had a small impact on the indices (correlations between old indices and new ones was higher or equal to 0.92**) and even less on the associated patterns (not shown).

The AMO indices reach the levels of 1950s in the last part of the 2000s. This is above the results obtained by Trenberth and Shea (2006) who showed for 2005 approximately 1/3 of the 1950s signal. This difference is due to the different methodology followed. We used EOFs calculated over the whole Atlantic instead of North Atlantic area averages. In addition, the use of low-frequency filtering with the end points reflected (like in Trenberth and Shea 2006) can be overly conservative in regions with high trends in the signals (Mann 2004), like the beginning of the 2000s.

Our study indicates a relative weak impact of the external (GW) forcing on the Sahelian rainfall variability compared to the natural (AMO, IPO). The GW contribution is only 10% on the 1980s drought. This is in contrast to findings of Held et al. (2005). The decline in Sahel rainfall in their model's ensemble mean is the result of anthropogenic forcing. Also the results of Biasutti and Giannini (2006) suggest a larger contribution of the external forcing on the drying (at least 30%).

As mentioned in the introduction, the AMO is generally understood as an internal physically consistent mode related to the oceanic thermohaline circulation (Knight et al. 2005). Nevertheless, our methodology for retrieving this signal cannot completely exclude the effect of external forcings, like aerosols, which have been shown to contribute to an asymmetrical SST warming pattern that could resemble the AMO (Rotstayn and Lohmann 2002). However, Ting et al. (2009) and Knight (2009) separated the internal component of the North Atlantic SSTs low-frequency variability. They used coupled models that took into account external forcings, including the effect of aerosols. Their results suggest that the greatest part of the AMO signal obtained here is related to the internal nature of the oscillation, especially in the North Atlantic, and that this component is highly related to Sahel rainfall multi-decadal variability (Ting et al. 2009).

Though we cannot rule out that some part of the external forcing is 'hidden' in our natural modes like the AMO, support to our findings comes from Hoerling et al. (2006). They cannot explain the pattern nor the amplitude of the Sahel drought by anthropogenic forcing.

The 2007 IPCC report points out that the studies disagree on which ocean basin is the dominant driver of the 1970–1980s Sahelian drought. E.g. Giannini et al. (2003) and Bader and Latif (2003) emphasize the role of the tropical Indian Ocean warming, whereas Hoerling et al. (2006) attribute the drying trend to a progressive warming of the South Atlantic relative to the North Atlantic. This study indicates that both oceanic regions are important. The GW and the IPO signal which are closely related to the tropical Indian and Pacific warming and the AMO which reflects the inter-hemispheric SST gradient in the Atlantic contribute more or less equal to the drought in the Sahel.

Regarding the simulations, it should be noted that the results obtained could be model dependent, particularly when addressing the role of the different basins. Nevertheless, they agree with the results from other studies in that the long-term trend of Sahel rainfall in the second half of the twentieth century was mainly driven by the tropical Indian and Pacific basins (Lu and Delworth 2005; Caminade and Terray 2009).

In this work we focused on the impact of SSTs on the West Africa Monsoon, so we have disregarded any other influence in our simulations. In particular, we have run all the experiments with fixed GHG. This is a limitation when comparing with observations because the impact of the SST pattern related to the GW was experienced in the 'real world' associated with an increase of these gases (Trenberth et al. 2007). Additional experiments (not shown) showed that when taking into account the whole GW signal (SST pattern plus increased GHG), the magnitude of Sahel drought is 30–40% smaller than the one obtained with only the SST pattern. The change in GHG from 1910 to 2008 warms the tropical atmosphere and increases surface temperatures over the Sahara (not shown). This, in turn, increases the heat low, favouring more rainfall over the Sahel, in consistency with Haarsma et al. (2005). This effect works against the drought due to the warming of the tropical SSTs and explains the reduction in drought for the whole GW signal (SST pattern plus GHG).

7 Summary and conclusions

In this work we investigated the relationship between the evolution of summer rainfall over West Africa in the twentieth century and the low-frequency SST variability. Unlike other studies, we have decomposed the low-frequency SST variability in two time-scales. We have shown that observed precipitation over West Africa was statistically linked to the long-term warming trend of SSTs (GW), which was mainly controlled by external (natural and anthropogenic) forcing. It was also related to the IPO and AMO decadal and multi-decadal variability components. We have also taken into account decadal variability in the Indian Ocean. Nevertheless, we have shown that this variability could be reconstructed from the information contained in the global AMO and IPO indices and patterns.

To further analyse the relationship of Sahel rainfall with the GW, the AMO and the IPO we have used the LMDZ

Table 5 Summary table with the impact of each component of SST low-frequency variability on West Africa rainfall

Component	Impact on West Africa	SST key areas	Mechanism	Contribution to 1980s drought (%)	Contribution to mid-1990s recovery (%)
GW	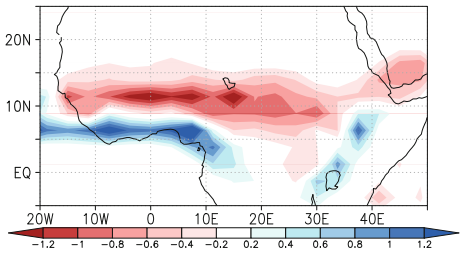	Tropical Indo-Pacific Tropical Atlantic	Enhanced subsidence over West Africa Increased humidity fluxes into Guinea Gulf	10	−20
AMO	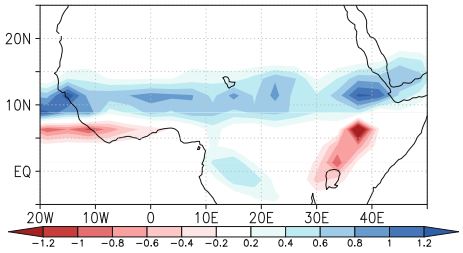	Atlantic + Mediterranean + Tropical Indian + Maritime Continent	Northward shift of the ITCZ	50	80
IPO	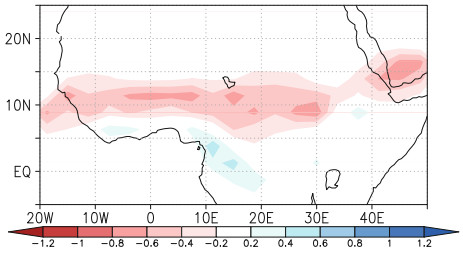	Tropics	Enhanced subsidence over West Africa	40	40

The second column plots the average impact using ERSSTv3 and HadISST1 simulations (mm/day). The SST key areas with impact on West African rainfall and the mechanism for the connection are shown in columns third and fourth. Columns fifth and sixth show the relative contribution of each component to Sahel's drought in the 1980s and to its partial recovery in the mid 1990s

model. Table 5 synthesises the main contribution of each component to Sahel rainfall low-frequency variability.

Regarding the long-term trend, the GW simulations show the biggest impact over West Africa, with a zonally elongated drying over the Sahel and enhanced precipitation over the Guinea Gulf (Table 5). It is associated with anomalous subsidence over West Africa, a decrease of monsoon strength and a southward shift of the ITCZ. Circulation and rainfall anomalies are mainly controlled by the tropical warming of SSTs. The anomalies of SST over Atlantic and Indian basins related to this pattern are responsible for most of the precipitation pattern over West Africa. Warm anomalies over the tropical Atlantic increase rainfall over Guinea Gulf and weaken the monsoon's westerlies. The warming over the Indian Ocean produces subsidence over the western part of West Africa and controls most of the drying over the western Sahel. The anomalies over the tropical Pacific in the GW pattern induce subsidence over eastern Africa and are responsible for the drying over the eastern Sahel.

The positive phase of the AMO enhances precipitation over the Sahel and decreases it over the Guinea Gulf (Table 5). It also shifts northwards the ITCZ. The tropical AMO SSTs cannot account for the anomalies of precipitation over West Africa. Note that neither can the Atlantic by its own, which agrees with simulations performed by other groups that used only the Atlantic part of the AMO signal (Sutton and Hodson 2005; Hodson et al. 2009). Instead, the Atlantic plus Mediterranean basins control the overall precipitation structure. Nevertheless, they can only account for approximately 60% of precipitation anomalies over the Sahel. Though weak, the SST cooling over the Indian basin (including the Maritime Continent) is needed to retrieve most of the precipitation enhancement over the Sahel.

Regarding the IPO, our simulations show that it impacts West Africa causing a decrease of precipitation over the Sahel (Table 5). Our simulations also suggest that the main effect is due to the tropical SSTs linked to the IPO signal. Note that the Pacific SSTs alone cannot simulate the overall IPO impact on West Africa.

Therefore, our results suggest that we can interpret SST-driven decadal evolution of Sahel precipitation in the twentieth century as the result of three competing factors: the GW, AMO and IPO. Following this interpretation, our results show that the SST-driven Sahel drought of the 1980s was mainly controlled by the AMO component of SSTs decadal variability rather than the long-term warming trend (GW) (Table 5). They also support the hypothesis that the recent partial recovery of Sahel rainfall is mainly due to the AMO, counteracted by the quick increase in tropical SSTs due to the GW.

Predictability of the IPO is still not possible because the actual mechanism for this phenomenon is still under debate (Mantua and Hare 2002). For the AMO there are some predictions that point to a change to a negative phase in the next few decades (Knight et al. 2005). If this were so, the combined effect of a negative AMO and an increased GW could lead in the future to a bigger drought in the Sahel than in the 1980s. Nevertheless, these predictions should be taken with care, because they are based on an analysis that considers only the effect of decadal to multi-decadal variability of SSTs. There are other sources of variability that could affect Sahel rainfall, like land-surface processes or GHG. We have shown that, in agreement with Haarsma et al. (2005) and Giannini (2009), the latter have a positive impact on Sahel rainfall, so their increase in the following years could partially counteract the negative trends due to SSTs. In addition, the relationship between SSTs and Sahel rainfall could be non stationary (Biasutti et al. 2008).

Acknowledgments We would like to thank the anonymous reviewers for their helpful comments, which greatly helped to improve the manuscript. This work was supported by the POSDEXT-MEC programme of the Spanish Ministry for Science and Innovation and by the COMPAS and DecCen project funded by the research council of Norway. Additional support was provided by the Spanish projects: MICINN CGL2009-10285 and MARM MOVAC 200800050084028. This work was carried out in the framework of the AMMA-EU project. Based on French initiative, AMMA was built by an international scientific group and is currently funded by a large number of agencies, especially form France, UK, US and Africa. It has been beneficiary of a major financial contribution from the European Community's Sixth Framework Research Programme. Detailed information on scientific coordination and funding is available on the AMMA International website http://www.amma-international.org.

References

Adler RF, Huffman GJ, Chang A, Ferraro R, Xie P, Janowiak J, Rudolf B, Schneider U, Curtis S, Bolvin D, Gruber A, Susskind J, Arkin P (2003) The Version 2 Global Precipitation Climatology Project (GPCP) Monthly Precipitation Analysis (1979-present). J Hydrometeorol 4:1147–1167

Ashok K, Chan WL, Motoi T, Yamagata T (2004) Decadal variability of the Indian Ocean dipole. Geophys Res Lett 31:L24207. doi:10.1029/2004GL021345

Bader J, Latif M (2003) The impact of decadal scale Indian Ocean SST anomalies on Sahelian rainfall and the North Atlantic Oscillation. Geophys Res Lett 30:2169. doi:10.1029/2003GL018426

Baines PG, Folland CK (2007) Evidence for a rapid global climate shift across the late 1960s. J Clim 20:2721–2744. doi:10.1175/JCLI4177.1

Barnett TP, Pierce DW, AchutaRao KM, Gleckler PJ, Santer BD, Gregory JM, Washington WM (2005) Penetration of human-induced warming into the world's oceans. Science 309:284–287

Biasutti M, Giannini A (2006) Robust Sahel drying in response to late 20th century forcings. Geophys Res Lett 33:L11706. doi:10.1029/2006GL026067

Biasutti M, Held IM, Sobel AH, Giannini A (2008) SST forcings and Sahel rainfall variability in simulations of the twentieth and twenty-first centuries. J Clim 21:3471–3486

Bony S, Emanuel JL (2001) A parameterization of the cloudiness associated with cumulus convection; evaluation using TOGA COARE data. J Atmos Sci 58:3158–3183

Bretherton CS, Widmann M, Dymnikov VP, Wallace JM, Bladé I (1999) The effective number of spatial degrees of freedom of a time-varying field. J Clim 12:1990–2009

Cai W, Whetton PH (2001) Modes of SST variability and the fluctuation of global mean temperature. Clim Dyn 17:889–901

Caminade C, Terray L (2009) Twentieth century Sahel rainfall variability as simulated by the ARPEGE AGCM, and future changes. Clim Dyn. doi:10.1007/s00382-009-0545-4

Cole JE, Dunbar RB, McClanahan TR, Muthiga NA (2000) Tropical Pacific forcing of decadal SST variability in the western Indian Ocean over the past two centuries. Science 287:617–619

Crowley TJ (2000) Causes of climate change over the past 1000 years. Science 289:270–277

Crueger T, Zinke J, Pfeiffer M (2009) Patterns of Pacific decadal variability recorded by Indian Ocean corals. Int J Earth Sci 98:41–52

Desser C, Phillips AS, Hurrel JW (2004) Pacific interdecadal climate variability: linkages between the Tropics and the North Pacific during boreal winter since 1900. J Clim 17:3109–3124

Dima M, Lohmann G (2007) A hemispheric mechanism for the Atlantic Multidecadal Oscillation. J Clim 20:2706–2719. doi:10.1175/JCLI4174.1

Emanuel KA (1991) A scheme for representing cumulus convection in large-scale models. J Atmos Sci 48:2313–2335

Emanuel KA (1993) A cumulus representation based on the episodic mixing model; the importance of mixing and microphysics in predicting humidity. AMS Meteorol Monogr 24:185–192

Falvey M, Garreaud RD (2009) Regional cooling in a warming world: recent temperature trends in the southeast Pacific and along the west coast of subtropical South America (1979–2006). J Geophys Res 114. doi:10.1029/2008JD010519

Fiorino (2000) Web document: http://www-pcmdi.llnl.gov/projects/amip/AMIP2EXPDSN/BCS_OBS/amip2_bcs.htm

Folland CK, Parker DE (1995) Corrections of instrumental biases in historical sea surface temperature data. Q J R Meteorol Soc 121:319–367

Folland CK, Palmer TN, Parker DE (1986) Sahel rainfall and worldwide sea temperatures, 1901–85. Nature 320:602–607. doi:10.1038/320602a0

Fontaine B, Trzaska S, Janicot S (1998) Evolution of the relationship between near global and Atlantic SST modes and the rainy season in West Africa: statistical analyses and sensitivity experiments. Clim Dyn 14:353–368

Fontaine B, Garcia-Serrano J, Roucou P, Rodriguez-Fonseca B, Losada T, Chauvin F, Gervois S, Sijikumar S, Ruti P, Janicot S (2009) Impacts of warm and cold situations in the Mediterranean basins on the West African monsoon: observed connection patterns (1979–2006) and climate simulations. Clim Dyn. doi:10.1007/s00382-009-0599-3

Giannini A (2009) Mechanisms of climate change in the semi-arid African Sahel: the local view. J Clim. doi:10.1175/2009JCLI3123.1

Giannini A, Saravannan R, Chang P (2003) Oceanic forcing of Sahel rainfall on interannual to interdecadal time scales. Science 302:1027–1030

Haarsma RJ, Selten FM, Weber SL, Kliphuis M (2005) Sahel rainfall variability and response to greenhouse warming. Geophys Res Lett 32:L17702. doi:10.1029/2005GL023232

Hagos S, Cook K (2008) Ocean warming and late-twentieth-century Sahel drought and recovery. J Clim 21:3797–3814. doi:10.1175/2008JCLI2055.1

Hansen J, Nazarenko L, Ruedy R, Sato M, Willis J, Del Genio A, Koch D, Lacis A, Lo K, Menon S, Novakov T, Perlwitz J, Russell G, Schmidt GA, Tausnev N (2005) Earth's energy imbalance: confirmation and implications. Science 308:1431–1435

Hansen J, Sato M, Ruedy R, Lo K, Lea D, Medina-Elizade M (2006) Global temperature change. PNAS 103:14288–14293

Held IM, Delworth TL, Lu J, Findell KL, Knutson TR (2005) Simulation of Sahel drought in the 20th and 21st centuries. PNAS 102:17891–17896

Hodson DLR, Sutton RT, Cassou C, Keenlyside N, Okumura Y, Zhou T (2009) Climate impacts of recent multidecadal changes in Atlantic Ocean Sea Surface Temperature: a multimodel comparison. Clim Dyn. doi:10.1007/s00382-009-0571-2

Hoerling M, Hurrell JW, Eischeid J, Phillips AS (2006) Detection and attribution of twentieth-century northern and southern African rainfall change. J Clim 19:3989–4008

Hourdin F, Musat I, Bony S, Braconnot P, Codron F, Dufresne JL, Fairhead L, Filiberti MA, Friedlingstein P, Grandpeix JY, Krinner G, LeVan P, Li ZX, Lott F (2006) The LMDZ4 general circulation model: climate performance and sensitivity to parametrized physics with emphasis on tropical convection. Clim Dyn 27:787–813

Joly M (2008) Rôle des océans dans la variabilité climatique de la Mousson Africaine. Dissertation, Université Paris-Est

Jung T, Ferranti L, Tompkins AM (2006) Response to the summer of 2003 Mediterranean SST anomalies over Europe and Africa. J Clim 19:5439–5454

Kerr RA (2000) A North Atlantic climate pacemaker for the centuries. Science 288:1984–1985

Knight JR (2009) The Atlantic multidecadal oscillation inferred from the forced climate response in coupled general circulation models. J Clim 22:1610–1625. doi:10.1175/2008JCLI2628.1

Knight JR, Allan RJ, Folland CK, Vellinga M, Mann ME (2005) A signature of persistent natural thermohaline circulation cycles in observed climate. Geophys Res Lett 32. doi:10.1029/2005GL024233

Knight JR, Folland CK, Scaife AA (2006) Climate impacts of the Atlantic multidecadal oscillation. Geophys Res Lett 33. doi:10.1029/2006GL026242

Koster R, Dirmeyer P, Cuo Z, Bonan C, Chan E, Cox P, Gordon C, Kanae S, Kowalczyk E, Lawrence D, Liu P, Lu C, Malyshev S, McAvaney B, Mitchell K, Mocko D, Oki T, Oleson K, Pitman A, Sud Y (2004) Regions of strong coupling between soil moisture and precipitation. Science 305(5687):1138–1140

Krishnan R, Sugi M (2003) Pacific decadal oscillation and variability of the Indian summer monsoon rainfall. Clim Dyn 21:233–242

Latif M, Keenlyside N, Bader J (2007) Tropical sea surface temperature, vertical wind shear, and hurricane development. Geophys Res Lett 34:L01710. doi:10.1029/2006GL027969

Lu J, Delworth TL (2005) Oceanic forcing of the late 20th century Sahel drought. Geophys Res Lett 32. doi:10.1029/2005GL023316

Lu R, Dong B (2008) Response of the Asian summer monsoon to weakening of Atlantic thermohaline circulation. Adv Atmos Sci 25:723–736

Mann ME (2004) On smoothing potentially non-stationary climate time series. Geophys Res Lett 31. doi:10.1029/2004GL019569

Mann ME (2008) Smoothing of climate time series revisited. Geophys Res Lett 35. doi:10.1029/2008GL034716

Mantua NJ, Hare SR (2002) The Pacific decadal oscillation. J Oceanogr 58:35–44

Mantua NJ, Hare SR, Zhang Y, Wallace JM, Francis RC (1997) A Pacific interdecadal climate oscillation with impacts on Salmon production. Bull Am Meteorol Soc 78:1069–1079

Meehl GA, Hu A (2006) Megadroughts in the Indian Monsoon region and southwest North America and a mechanism for associated multidecadal Pacific sea surface temperature anomalies. J Clim 19:1605–1623

Meehl GA, Washington WM, Ammann CM, Arblaster JM, Wigley TML, Tebaldi C (2004) Combinations of natural and anthropogenic forcings in twentieth-century climate. J Clim 17:3721–3727

Meehl GA, Stocker TF, Collins WD, Friedlingstein P, Gaye AT, Gregory JM, Kitoh A, Knutti R, Murphy JM, Noda A, Raper SCB, Watterson IG, Weaver AJ Zhao ZC (2007) Global climate projections. In: Solomon S, Qin D, Manning M, Chen Z, Marquis M, Averyt KB, Tignor M, Miller HL (eds) Climate Change 2007: the physical science basis. Contribution of Working Group I to the Fourth Assessment Report of the Intergovernmental Panel on Climate Change. Cambridge University Press, Cambridge

Meehl GA, Hu A, Santer BD (2009) The mod-1970s climate shift in the Pacific and the relative roles of forced versus inherent decadal variability. J Clim 22:780–792

Miller AJ, Cayan DR, Barnett TP, Graham NE, Oberhuber JM (1994) The 1979–77 climate shift of the Pacific Ocean. Oceanography 7:21–26

Mitchel TD, Jones PD (2005) An improved method of constructing a database of monthly climate observations and associated high-resolution grids. Int J Climatol 25:693–712. doi:10.1002/joc.1181

North GR, Bell TL, Cahalan RF (1982) Sampling errors in the estimation of empirical orthogonal functions. Mon Weather Rev 110:699–706

Palmer TN (1986) Influence of the Atlantic, Pacific, and Indian Oceans on Sahel rainfall. Nature 322:251–253

Polyakov IV, Alexeev A, Bhatt US, Polyakova EI, Zhang X (2009) North Atlantic warming: patterns of long-term trend and multidecadal variability. Clim Dyn. doi:10.1007/s00382-008-0522-3

Power S, Casey T, Folland C, Colman A, Mehta V (1999) Inter-decadal modulation of the impact of ENSO on Australia. Clim Dyn 15:319–324

Rayner NA, Parker DE, Horton EB, Folland CK, Alexander LV, Rowell DP (2003) Global analyses of sea surface temperature, sea ice, and night marine air temperature since the nineteenth century. J Geophys Res 108. doi:10.1029/2002JD002670

Rotstayn LD, Lohmann U (2002) Tropical rainfall trends and the indirect aerosol effect. J Clim 15:2103–2116

Rowell DP (2003) The impact of the Mediterranean SSTs on the Sahelian rainfall season. J Clim 16:849–862

Rowell DP, Folland CK, Maskell K, Owen JA, Ward NM (1992) Modelling the influence of global sea surface temperatures on the variability and predictability of seasonal Sahel rainfall. Geophys Res Lett 19:905–908

Rowell DP, Folland CK, Maskell K, Ward NM (1995) Variability of summer rainfall over tropical North Africa (1906–92): observations and modelling. Q J R Meteorol Soc 121:669–704

Scott PA, Tett SFB, Jones GS, Allen MR, Mitchell JFB, Jenckins GJ (2000) External control of 20th century temperature by natural and anthropogenic forcings. Science 290:2133–2137

Shanahan TM, Overpeck JT, Anchukatis KJ, Beck JW, Cole JE, Dettman DL, Peck JA, Scholz CA, King JW (2009) Atlantic forcing of persistent drought in West Africa. Science 324:377–380

Smith TM, Reynolds RW (2002) Bias corrections for historical sea surface temperatures based on marine air temperatures. J Clim 15:73–87

Smith TM, Reynolds RW, Peterson TC, Lawrimore J (2008) Improvements to NOAA's historical merged land-ocean surface temperature analysis (1880–2006). J Clim 21:2283–2296. doi:10.1175/2007JCLI2100.1

Sutton RT, Hodson DLR (2005) Atlantic Ocean forcing of North American and European summer climate. Science 309:115–118

Thompson DWJ, Kennedy JJ, Wallace JM, Jones PD (2008) A large discontinuity in the mid-twentieth century in observed global-mean surface temperature. Nature 453:646–649. doi:10.1038/nature06982

Ting M, Kushnir Y, Seager R, Cuihua Li (2009) Forced and internal 20th century SST trends in the North Atlantic. J Clim 22:1469–1481

Tippet MK, Giannini A (2006) Potentially predicable components of African summer rainfall in an SST-forced GCM simulation. J Clim 19:3133–3144

Trenberth KE, Shea DJ (2006) Atlantic hurricanes and natural variability in 2005. Geophys Res Lett 33. doi:10.1029/2006GL026894

Trenberth KE, Jones PD, Ambenje P, Bojariu R, Easterling D, Klein Tank A, Parker D, Rahimzadeh F, Renwick JA, Rusticucci M, Soden B, Zhai P (2007) Observations: surface and atmospheric climate change. In: Solomon S, Qin D, Manning M, Chen Z, Marquis M, Averyt KB, Tignor M, Miller HL (eds) Climate change 2007: the physical science basis. Contribution of Working Group I to the Fourth Assessment Report of the Intergovernmental Panel on Climate Change. Cambridge University Press, Cambridge

Vecchi GA, Clement A, Solden BJ (2008) Examining the tropical Pacific's response to global warming. EOS 89(9):81–83

Worley SJ, Woodruff SD, Reynolds RW, Lubker SJ, Lott N (2005) ICOADS release 2.1 data and products. Int J Climatol 25:823–842

Yoshioka M, Mahowald NM, Conley AJ, Collins WD, Fillmore DW, Zender CS, Coleman DB (2007) Impact of desert dust radiative forcing on Sahel precipitation: relative importance of dust compared to sea surface temperature variations, vegetation changes and greenhouse gas warming. J Clim 20:1445–1467. doi:10.1175/JCLI4056.1

Zeng N, Neelin JD, Lau KM, Tucker CJ (1999) Enhancement of interdecadal climate variability in the Sahel by vegetation interaction. Science 286:1537–1540

Zhang R, Delworth TL (2006) Impact of Atlantic multidecadal oscillations on India/Sahel rainfall and Atlantic hurricanes. Geophys Res Lett 33. doi:10.1029/2006GL026267

Zhang Y, Wallace JM, Battisti DS (1997) ENSO-like interdecadal variability:1900–93. J Clim 10:1004–1020

Zhou T, Yu R, Li H, Wang B (2008) Ocean forcing to changes in global monsoon precipitation over the recent half-century. J Clim 21:3833–3852. doi:10.1175/2008JCLI2067.1